Università degli Studi di Padova

Department of information Engineering

Master's Degree in Bioengineering for neurosciences

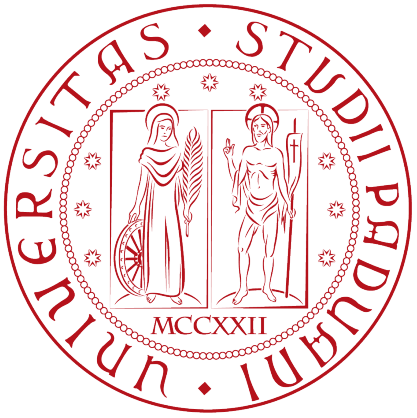

Exploratory study of the relationship between metrics derived from [18F]FDG PET and directed connectivity estimated from fMRI signals

Master's degree dissertation

Supervisor

Prof. Alessandra Bertoldo

Co-Supervisors

Eng.Giorgia Baron
Eng.Giulia Vallini

Master candidate

Andrea Bertola

Academic Year 2022-2023

27 November 2023

"The expert is a person who, in a very narrow field, has made all possible mistakes."

— Niels Bohr

Dedicated to my family and friends.

Abstract

In the intricate landscape of neuroscience, the exploration of brain connectivity has traditionally focused on understanding the functional and structural relationships among different brain regions. However, the brain's dynamic interplay between neural activity and energy metabolism, crucial for its optimal functioning, has given rise to a burgeoning field known as metabolic connectivity.

In this thesis we aim to explore a specific fusion approach that exploit a symmetric model-driven method such as DCM with FDG-PET connectivity maps from healthy subjects, characterizing the the overall network behaviour in terms of particular metrics that account for entropy variation. More over we will compare resulting relationship with respect of oncological patients.

"Shoot for the moon. Even if you miss, you will land among the stars."

— Normal Vincent Peale

Acknowledgements

First of all, I would like to express my gratitude to Prof. Alessandra Bertoldo, the supervisor of my thesis, for the help and support provided to me during the drafting of the work. Her dedication to her work has been a stimulus and inspiration for me. also want to thank my co-supervisors, Engineer Giorgia Baron and Engineer Giulia Vallini, who, with their dedication and patience, have accompanied me during these eight months.

I want to thank my parents and relatives for the constant support they have shown me throughout the entire course of my studies.

I want to thank my friends for these years spent together, for the diverse adventures we've experienced, and for the encouragement they have given me.

Padova, 27 November 2023 Andrea Bertola

Contents

List of Figures

List of Tables

Chapter 1

Introduction

In the intricate landscape of neuroscience, the exploration of brain connectivity has traditionally focused on understanding the functional and structural relationships among different brain regions. However, the brain's dynamic interplay between neural activity and energy metabolism, crucial for its optimal functioning, has given rise to a burgeoning field known as metabolic connectivity.[39] This emerging paradigm transcends traditional neuroimaging boundaries, offering a unique perspective into the energetic dialogue that underlies cognitive processes and forms the backbone of the brain's functional networks.At its essence, it delves into the intertwined relationship between neural activity and energy demands within the brain.

Metabolic connectivity characterizes the brain as a complex network of interconnected nodes and edges. In this context, nodes represent distinct brain regions, and edges signify the strength of metabolic coupling between them. The application of graph theoretical measures, such as degree centrality and efficiency, provides insights into the hierarchical organization of the brain's metabolic networks, shedding light on regions that play pivotal roles in energy distribution and information transfer. The implications of metabolic connectivity extend beyond the examination of resting-state networks. Task-related metabolic connectivity studies delve into how the brain dynamically allocates its energy resources in response to specific cognitive demands or external stimuli.[68] Whether unraveling the intricacies of memory formation, language processing, or emotional responses, task-related metabolic connectivity unveils the adaptability of the brain's energetic networks in supporting diverse cognitive functions.[41]

On the other hand, Blood oxygenation level-dependent fMRI has been heavily used as probe into functional brain connectivity characterization given the temporal coherence of low-frequency large-amplitude changes in BOLD signal.[79] Moreover it has been demonstrated its usefullness in the clinical field giving high sensitivity with respect to other conventional imaging methods.

That being the case , BOLD-fMRI provides a surrogate measure of neuronal activity with high spatial and temporal resolution but it could be affected by confounding effects generated by non-neuronal components.[89][68]

Despite both Metabolic connectivity and BOLD-fMRI represents powerful tools to grasp the interplay between neural activity and energy metabolism, the interpretation of activity-dependent glucose uptake remains intricate.Over the past decade,

two main theories regarding central nervous system (CNS) glucose metabolism have been vigorously debated.

The first theory, known as the Astrocyte-to-Neuron Lactate Shuttle Hypothesis (ANLSH), posits that energy metabolism is compartmentalized, with glycolysis outsourced to astrocytes.[32] Glucose is primarily taken up by astrocytes, converted to lactate through oxidative metabolism, and then utilized by neurons through mitochondrial lactate oxidation.[43] This hypothesis implies that glucose metabolism in activated brain regions only indirectly reflects neuronal metabolism, challenging the accuracy of functional brain imaging in representing neuronal activity.[55]

On the other hand, the Parsimonious Hypothesis (PH) proposes that neurons directly take up glucose from the interstitium and generate ATP through both glycolysis and oxidative metabolism. The ANLSH-PH debate has led to divergent views based on experimental studies.

Studies by Lundgaard et al. (2015)[55] have suggested that neurons, rather than astrocytes, are the primary consumers of glucose during rest and activity-dependent increases in neural activity. The evaluation of Hexose Kinases (HKs), considered gatekeeper enzymes in glycolysis, revealed consistently higher levels in neurons compared to astrocytes, supporting the idea that local neuronal glycolysis supports increased synaptic activity.

However, Patel et al. (2014)[1] argued against the ANLSH, presenting evidence that neuronal glucose-derived pyruvate, not lactate from astrocytes, is the major oxidative fuel for activated neurons. These conflicting findings highlight the complexity of CNS glucose metabolism.

Recent studies propose a middle-ground interpretation, suggesting that under resting conditions, brain metabolism occurs almost exclusively through complete oxidative metabolism of glucose in both neurons and astrocytes. The glutamate-glutamine cycle facilitates interaction between these cell types, confirming the compartmentalization of metabolic processes.[9][4]

Moving from the cellular level to noninvasive imaging methods, functional Magnetic Resonance Imaging (fMRI) and [^{18}F]Fluorodeoxyglucose Positron Emission Tomography (FDG-PET) have provided valuable insights into functional and metabolic coupling in the brain. Starting from the concept of the Human Connectom as an extensive map of neural connections, studies have revealed coordinated activation of local neural circuits, forming functional brain networks. However, the relationship between specific tasks, functional brain networks, and metabolic processes remains an ongoing area of investigation.[86][85]

Recent advancements in FDG-PET and fMRI have demonstrated their complementary nature in understanding neural mechanisms.[68] The introduction of measures like the Metabolic Connectome Mapping (MCM) has allowed the integration of unidirectional functional connectivity with local energy metabolism (Riedl et al., 2016)[117]. Studies have also unveiled bidirectional and unidirectional signaling across the cortex, highlighting changes in network interactions across different brain states.

Despite the controversies and discrepancies in findings, the integration of FDG-PET and fMRI has shown promise in uncovering the complexities of neural function and metabolism. These multimodal imaging approaches offer unique advantages, emphasizing the need for a comprehensive understanding of the brain's intricate

processes.
Latest innovation proposed simultaneous PET/MR acquisitions , however there are still some technical limitation to be improved indeed image artifacts or decrease signal-to-noise ration can be caused by induced eddy currents in the PET shielding therefore interfering with B_0 field homogenity. Despite the technical demands underlying the "matchmaking" between PET and MR, the differences between these two partners is the greatest source of strength in their potential marriage.[24]
Another emerging approach in connectivity field exploits data fusion between the two thereof modalities. As stated by *Jamadar* [100] quantitative or calibrated fMRI toghether with MR-PET or PET techniques , have the potential to offer additional insights into the shift between neaural energy sources and the relative utility of glucose and oxygen cerebral metabolic processes. These approaches have indeed shown improved ability to uncover latent relationship between data types and currently there are four main methods for data fusion. [116] Many studies use a qualitative visual comparison which can be very informative despite non allowing quantitative inference . Most existing existing BOLD-fMRI/FDG-PET studies use a data integration approach, where data from each modality is analysed separately and compared at the second-level using correlation [52][7] or similarity metrics [13]. Particular cautions is needed if asymmetric data fusion is intended to be used where information from one modality constraint the other as it could impose unrealistic assumptions and also bias the analysis.[100] Therefore the emerging field of integrated FDG-PET/fMRI holds great potential for advancing neuroscience research and providing a deeper understanding of the interplay between neural activity and metabolism.

In this thesis we aim to explore a specific fusion approach that exploit a symmetric model-driven method such as DCM with FDG-PET connectivity maps from healthy subjects, characterizing the the overall network behaviour in terms of particular metrics that account for entropy variation. More over we will compare resulting relationship with respect of oncological patients.

The first three chapter are an explanation on the key concepts used in this dissertation , organized as follow:

* *Chapter1*: gives a general introductions about key concept used in this thesis. 1

* *Chapter2*: defines key concepts like SUVR and reviews the genesis of metabolic connectivity. It discusses main approaches like seed correlation, ICA/PCA, graphical lasso, and graph theory. 2

* *Chapter3*: introduces dynamic causal modelling (DCM) as a framework to estimate effective connectivity from neuroimaging time series. It details the bilinear state space model combining neuronal and hemodynamic models. It also presents sparse DCM, which estimates whole-brain effective connectivity from resting-state fMRI.n. 3

The last four chapter are dedicated to the experiment explanation, divided in :

* *Chapter4*: describes the healthy and oncological datasets, acquisition protocols, preprocessing steps, and the reference atlas used. It explains how effective connectivity, metabolic connectivity, and SUVR matrices were estimated..

* *Chapter5*: presents the results. It shows the choice of noise variance in sparse DCM. It analyzes correlations between derived metrics and finds consistent relationships. It uses Wilcoxon tests to compare healthy and oncological correlations. It isolates network contributions to specific correlations.

* *Chapter6*: discusses key findings. It analyzes the noise variance selection and correlation results. It interprets network contribution analyses and group-level differences. It acknowledges limitations like residual noise and tumor effects.

* *Chapter7*: gives final conclusion. Highliting main limitations and proposing future research topics

Chapter 2

Metabolic Connectivity

2.1 Standardized Uptake Value Ratio

The standardized uptake value (SUV) is a dimensionless ration used to distinguish between "normal" and "abnormal" levels of uptake thus being utilized in positron emission tomography(PET) as well as in modern calibrated single photon emission tomography (SPECT). This measure is common in the clinical field especially in the analysis [18F]fluorodeoxyglucose ([^{18}F]FDG) images of cancer patients and it could be also be used in combination with other PET agents when no *arterial input function* is aviable for more detailed pharmacokinetic modelling.
Originally it was designed to be a simplistic method to quantify uptake as opposed to true quantification through compartmental and kinetic modelling and clinically exploited to determine whether a region could be considered "tumor" or "malignat" but may have limited value for determining the edges of a tumor.[87]

Many factors affect SUV measure, including accuracy of dose calibration, time between injection and imaging (dose to scan time), patient weight (changes common in oncology patient), motion artifacts and blood glucose level indeed SUV is dependent on many patient-related as well as procedural factors such as definition of ROIs , competition with endogenous glucose , rate of phosphorylation , body size and composition as well as tumor type.[33] Technically, SUV values would vary depending on PET scanner's signal-to-noise properties , the accuracy oh the image reconstruction algorithm as well as corrections algorithms. Not accounting for all these factos can lead to potential errors of $\geq$50% in SUV calculations.

It is defined as the ratio of activity per unit volume of a region of interest(ROI) to the activity per unit whole body volume or alternately as ratio of the radiotracer concentration c_{rad} (kBq/ml) and the whole body concentration of the injected tracer c_{inj} .

$$SUV = \frac{c_{rad}(kBq/ml)}{c_{inj}} \tag{2.1}$$

Injection The c_{inj} value is calculated as ration of two independent measurements : the injected tracer (injected dose ID) and the subject-specific factor a where it

can be expressed in terms of body weight (BW), surface area or lean body mass. The ID can be estimated as difference in the radioactivity of the syringe before and after injection , if considered necessary with correction for physical decay between each measurements and the time of injection. Usually the time of injection is $t = 0$, This reference concentration represents the supposed even distribution of the injected radiotracer across the whole body .

Tackling the problem of nuance factors *Boellaard et al.* [91] showed how simple SUV depended strongly on patient-related metrics therefore making suitable its use only for diagnostic purposes when data acquisition and processing are performed in a standardized way. Contrary to that SUV rations depend less on noise and image resolution and therefore are more suitable for multicenter studies.
Finally, when considering the SUV from two different region whithin the same PET image thus applying a sort of reference-based approach we have to define what is termed as standardized uptake value ratio (SUVR). For the SUVR , the injected radiotracer , the body weight and the mass density that are all part of the SUV calculation , cancel:

$$SUVR = \frac{SUV_{target}}{SUV_{reference}} = \frac{c_{img,target}}{c_{img,reference}} \tag{2.2}$$

2.2 The genesis of Metabolic Coneectivity

In the last forty years [^{18}F]-fluordeoxy-glucose (FDG) has become increasingly considered in the research as well as in the clinical world.
Unlike the BOLD fMRI, PET measurements are deemed indicative of a presumed steady state of neuronal activity during the recording interval for several reasons. PET imaging, employing radiotracers like fluorodeoxyglucose ([^{18}F]FDG), captures brain activity over a relatively extended time scale, encompassing the administration, distribution, and accumulation of the radiotracer, as well as the subsequent decay of the radioisotope. This prolonged timeframe results in a more averaged and sustained representation of neuronal activity, contributing to the perception of a steady state. The radiotracer kinetics, mirroring the metabolic pathways of substances like glucose, entail processes such as uptake, phosphorylation, and entrapment in tissues, further emphasizing the temporal characteristics of PET measurements. Additionally, PET measurements, rooted in metabolic processes, particularly glucose utilization, are closely tied to cellular energy demands, including those of neurons. This metabolic stability implies that PET captures a state where overall metabolic requirements remain relatively constant, indicating a presumed steady state of neuronal activity. Notably, PET measurements are less sensitive to rapid and transient changes associated with neurovascular coupling, making them suitable for probing more sustained facets of brain function and metabolism.
This immunity from post-capillary down-stream vascular noise together with the high count rate in [^{18}F]FDG-PET recording from brain, may contribute to the robustness and reproducibility of [^{18}F]FDG-PET findings at a single subject level.

When this field had yet to emerge *Clark and Stoessl* [30] in a proof of concept

, suggested how the analysis merely focused on regional variation of cerebral metabolic rate of glucose (CMRGlu) woldn't be enough to highlight changes in regional relationship. At that time such changes were examined by testing for covariance or correlations between brain regions where inter-regional covariance were specifically explored using multivariate techniques such as PCA, factor analysis and subscale subprofile model (SSM). [25][61]
The concept of "*Metabolic Connectivity*" arose with *Horwitz et al.,1984* [21] and later on named by *Lee et al.,2008* [39] where using a voxel-wise interregional correlation analysis (IRCA) they examined resting brain connectivity.

2.3 Main approaches of metabolic connectivity

Hitherto countless statistical methods or frameworks has been developed with the intention of capturing metabolic connectivity . Despite being originated form group based data analysis , it has to be noted that the thereof method can support making inference at a single subject level.

The main approaches on MC include:

1. **Seed correlation (SCA)** : which consist in defining a reference region and computing correlation with glucose rediotracer uptake for every other brain voxel

2. **PCA** or **ICA**: ICA optimizes higher-order statistics such as kurtosis and it is used to retrive independent component . PCA optimizes the covariance matric of the data which is a second-order statistic and it is used to find uncorrelated components. So they can be considered as multivariate decompositions that impose constrains of orthogonality and statistical independence on derived components.

3. **Sparse inverse covariance estimation(SICE)**: also known as graphical lasso in which one approaches the true undelying connectivity matrix and simultaneusly imposes sparsity[1] (proportion of zero-entry) to increase statistical robustness in the face of a low number of observations.

4. **Graph theory**: a popular framework in wich sparsity is imposed by thresholding the pair-wise correlation values to form binary adjacency matrices.

Recently has been presented an extensive comparison work by *Volpi et al.2021* [112]

[1] In numerical analysis and scientific computing, a sparse matrix or sparse array is a matrix in which most of the elements are zero. There is no strict definition regarding the proportion of zero-value elements for a matrix to qualify as sparse but a common criterion is that the number of non-zero elements is roughly equal to the number of rows or columns. By contrast, if most of the elements are non-zero, the matrix is considered dense. The number of zero-valued elements divided by the total number of elements (e.g., m × n for an m × n matrix) is sometimes referred to as the sparsity of the matrix.

for SICE and non-SICE approach with the aim to derive MC at single subject-level. They compared with SC four approaches to estimate sparse inverse covariance matrices as well as three similarity-based methods to derive adjacency matrices. The metrics and approaches that they considered included: *bivariate Pearson's correlation coefficients***r**, *Euclidean distance*, *Cosine similarity* and SICE methods such as *DP-GLASSO*(See GLassoElnetFast R package [97]), *nonparanormal truncated* approach, *skeptic* method and the $\gamma - LASSO$.
In this work they also tackled different issues on behalf the thereof method's application moreover suggesting how Pearson's correlation, Euclidean distance and Cosine Similarity provided better results for between-subject reproducibility and similarity with Structural connectivity(Fig.4.3). Nevertheless most methods secceeded in retrieving a similar network structure, with consistent identification of inter-hemispheric and homotopic connections.

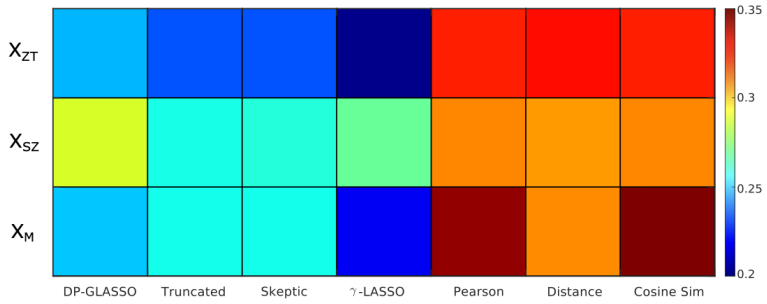

Figure 2.1: Dice similarity between binarized SC and median MC matrices. Dice similarity between binarized SC and median MC matrices (20% sparsity) for all standardization (rows) and MC estimation (columns) methods. (*Volpi et al.,2021*)[112]

Taking advantage on these conclusions *Volpi et al.*, in a subsequent work(*Volpi et al.,2023*)[113], tackled and reassessed the problem of validity and interpretability of Metabolic Connectivity inferred from either the covariation of static [^{18}F]FDG PET images across participants (*across-individual MC*(ai-MC)) or, as for rs-fMRI functional connectivity, from dynamic [^{18}F]FDG signals (*within-individual MC(wi-MC)*). By doing so they have proposed a novel wi-MC methodology that reassessed the concept of metabolic from a PET kinetic modelling perspective, estimating MC through a *Euclidean similarity* approach.(Fig.2.2)
In brief, PET data were first motion-corrected using FSL's *mcflirt*[80] and static PET image were generated by summing late frames after motion correction. The static PET image was afterwards linearly registered to T!w space and normalized into SUVR by dividing each voxel's value by the whole-brain [^{18}F]FDG average uptake. For PET kinetic modeling, an image-derived input function (IDIF) was extracted through a semi-automatic pipeline [42], including carotid artery segmentation, selection of "hot voxels", parametric clustering [38], and model fitting with spillover correction.[64]

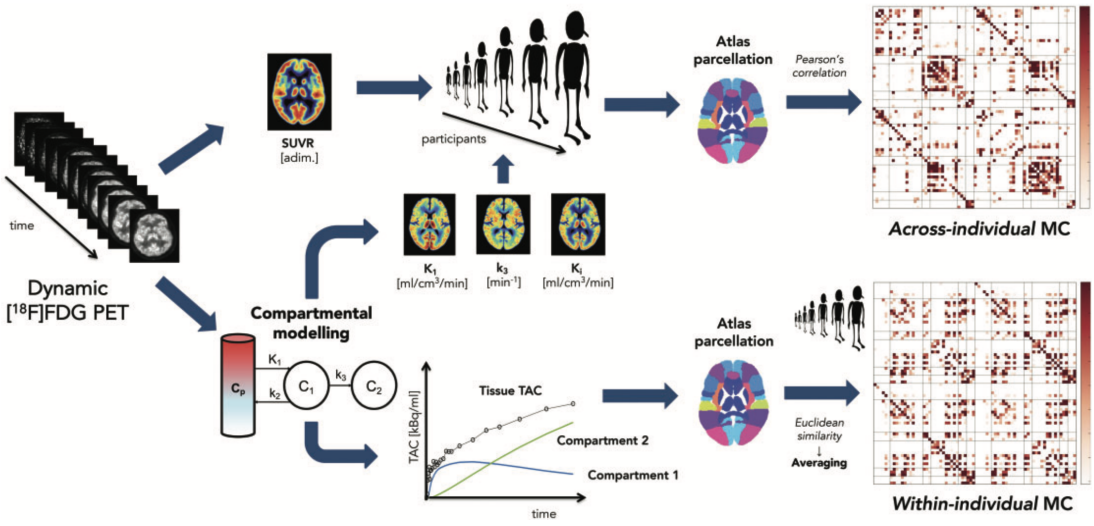

Figure 2.2: Analysis pipeline for inferring metabolic connectivity at the individual (within-individual approach) and group level (across-individual approach). [^{18}F]FDG PET dynamic data (far left) is the source of all inferences of metabolic connectivity. A static SUVR image (top left) is obtained from frames in the 40–60 min window of the dynamic PET data; in parallel, a two-tissue compartment model is fitted to dynamic PET data to estimate [^{18}F]FDG kinetic parameters at the voxel level (using Variational Bayesian inference and an image-derived input function as a surrogate for the [^{18}F]FDG plasma concentration C_p), in particular K_i, K_1 and k_3 (center), and reconstruct the time courses of compartments 1 and 2 (bottom center). From the subject series of SUVR, K_i, K_1 and k_3, parcellated thanks to the chosen atlas ROIs registered to individual PET space, we calculate across-individual MC via Pearson's correlation (top right), while from the time series of the tissue TACs, compartments 1 and 2, individual-level MC is obtained via Euclidean similarity and averaged across participants (bottom right). (*Volpi et al.,2023*)[113]

Voxel-wise estimation of Sokoloff's model parameters employed a Variational Bayesian approach, with k-means clustering applied to dynamic PET data. Parametric maps of K1, k2, k3, and Vb were obtained for each participant. The parametric map of K_i(irreversible tracer uptake) by solving at voxel level:

$$K_i = \frac{K_1 k_3}{k_2 + k_3} \tag{2.3}$$

The volxel-wise prediction of the time-varying free intracellular concentration of the [^{18}F]FDG tracer ($C_1(t)$) and its metabolized intracellular concentration ($C_2(t)$), was then reconstructed from Laplace transorm solution of Sokoloff'smodel by using IDIF as plasma function ($C_p(t)$)

$$\begin{aligned} C_1(t) &= \frac{K_1 k_2}{k_2 + k_3} e^{-(k_2+k_3)t} \otimes C_p(t) \\ C_2(t) &= K_i \int_0^t C_p(\tau) d\tau \end{aligned} \tag{2.4}$$

Finally, ROI-level PET signals ([^{18}F]FDG tissue TACs, $C_1(t)$ and $C_2(t)$) were temporally filtered, interpolated onto a uniform time-grid and wi-MC calculated with an *Euclidean similarity* approach.

Exploiting this framework for wi-MC estimates they were able to show the dissimilarity between ai-MC and wi-MC matrices and assess the higher matching pattern between FC derived matrix and wi-MC (Dice similarity: 0.47-0.63). Therefore demonstrating the feasibility of computing individual-level MC from dynamic PET and that it yields to interpretable matrices that bear similarity to fMRI FC measures.

Chapter 3

The Effective Connectivity

In the last decades the main forms of brain connectivity, which allows to characterize the interactions between brain regions, have been summerized in three groups:

* Anatomical or Structural Connectivity(SC) measures the density or probability of anatomical pathways that connect two brain areas. It is Aimed to provide a exhaustive description of the physical connections of the human nervous system.

* Functional Connectivity (FC) gives information about the temporal correlation in neuronal activation between spatially remote areas through the estimation of pairwise statistical dependencies.

* Effective Connectivity (EC)

Contrary to functional connectivity which captures patterns of statistical dependence, *effective connectivity* attempts to extract networks of causal influences of one neural element over another, hence highliting a directed connection . Various techniques for extracting effective connectivity have been pursued. One technique called "covariance structural equation modeling" assigns effective connection strengths to anatomical pathways that best match observed covariances in a given task (McIntosh and Gonzalez-Lima, 1994). A model-driven directed data fusion and generalization of this approach is called "Dynamic Causal Modelling (DCM)" has emerged as *Gold Standard* to estimate EC and was later extended with various considerations.

3.1 Dynamic Casual Modelling

The concept of Dynamic Causal Modelling (DCM) was introduced as series of procedures that deals with the interactions among neuronal population at a cortical level. Using neuroimaging time series, estimates the coupling between brain areas, giving an insight on how the coupling is affected by changes in the experimental evirorment.[15]
It can be considered as a *forward model* build on a nonlinear Multiple Input Multiple Output (MIMO) dynamical system that use a Byesian inference framework .The models are formulated in terms of differetial equations that represent the dymanic

of a hidden state in the nodes of a probabilistic graphical model , in which the conditional dependencies have to be cosidered in terms of ***effective connectivity***.

DCM principles Consider a MIMO with m inputs and l corresponding outputs (one for each region), where the m inputs are specific causes (e.g. stimulous functions) . Each input theoretically , could have direct access to every region but in practise the outward effects, related to inputs, are restricted to a single input region .
Given a set of m input each of the l regions produces a measurable output that corresponds to the observed BOLD signal, where each region is described by five state variables[1]. Only the first state variable of each region , though, has to be considered for the estimation of the effective connectivity due to the fact that these variables corresponds to neuronal or synaptic activity and are a function of the neuronal states of other brain regions.[15]

We will start by explaining some ground concepts which were refined in (*Friston et al.,2003*). First BOLD-fMRI specific equations for neuronal states and then we will have a look on the differential equations that constitute the hemodynamic model for each region.

3.1.1 Neuronal state equations

Recalling *Friston et. al. 2003*[15] , let us define the neuronal states $z = [z_1, \ldots, z_1]^T$ and the model for effective connectivity

$$\dot{z} = \mathbf{F}(z, u, \theta) \tag{3.1}$$

where $\mathbf{F}$ is a nonlinear function describing influences that activity z ,in all l brain region, and inputs u exert upon changes in the others. θ are parameters of the model whose posterior density we require for inference.
Considering a bilinear approximation of (3.1) we end up with a natural representation in terms of EC thus is not required to give a specific form to the function (3.1). The bilinear form is:

$$\dot{z} \approx Az + \sum_j u_j B^j z + Cu \quad = \quad (A + \sum_j u_j B^j)z + Cu \tag{3.2}$$

where we have considered a bilinear low-order Taylor approximation to account for both endogenous and exogenous causes of system dynamics, where:

$$A = \frac{\partial \mathbf{F}}{\partial z} = \frac{\partial \dot{z}}{\partial z} \qquad B^j = \frac{\partial^2 \mathbf{F}}{\partial z \partial u_j} = \frac{\partial}{\partial u_j}\frac{\partial \dot{z}}{\partial z} \qquad C = \frac{\partial \mathbf{F}}{\partial u} \tag{3.3}$$

The matrix A known as connectivity matrix represents the first order connectivity among brain region in condition of absence of external stimuli .We can think of EC

[1]Four state variables (vasodilatory signal, normalised flow, normalised venous volume and normalised deoxyhemoglobin content) ,representing the hemodynamic states, are required to compute the BOLD signal itself and are not effected by states of other regions.

as the influence of a neuronal region over another in terms of inducing a response $\frac{\partial \dot{z}}{\partial z}$ thus changing the neuronal state.
Therefore considering the DCM procedure we recognise the response in an activity change over time $\dot{z}$ and it can be thought as intrinsic coupling in absence of experimental perturbations.[2]
The matrices B^j are the actual change in coupling iduced by the j-th input, thus they encode the modulation over the instrinsic coupling itself and are obtained from manipulations of the experimental envirorment or setup. We refer to B^j as bilinear given that includes a secon-order differential term.
On bealf of C matrix , it represent input-driven influences on the neural activity .
In the idenfitifation phase we would identify the parameters $\theta^c = \{A, B^j, C\}$ and define the functional architecture and connections among brain region thus describing the model at neuronal level.

In a subsequent study the original equation(3.2) was characterized in order to deal with resting-state fMRI (*Friston et al.,2014* [67]). In this setting, external stimuli are absent , that is $u(t) = 0$ and the random fluctuations associated with the neural state are responsible for driving the neural activity. Therefore, the neural state equation (3.1) beacomes linear and can be expressed as :

$$\dot{x}(t) = Ax(t) + \nu(t) \tag{3.4}$$

with A representing effective connectivity and $\nu(t)$ the random fluctuations associated to the neural state.
This formulation for rs-fMRI was later exploited in section (3.2).

3.1.2 Hemodynamic state equations

The DCM procedure combines the presented bilinear model of neuronal connectome dynamics with a validated hemodynamic model that describes the transition from neuronal activity to a BOLD observable response .In brief, neuronal state changes drive local changes in blood flow, which inflates blood volume and reduces deoxyhemoglobin content.
The so-called *"Balloon Model"* , also known as *Balloon-Windkessel model*, was fist introduced by *Bruxton et al.,1998* [14] and later extended in *Friston et al.,2000* [16].
Therefore to describe the remaining four state variables , which consitute the BOLD signal and rule the transition from neuronal activity to observable hemodynamic response, in *Friston et al.,2006* [15] it has been expoited the Balloon model as follow.

For the *i-th* region a significant neuronal activity z_i increases the vasodilatory signal s_i that is subject to auto regolatory feedback .
Incoming fluxes f_i responds proportionally to s_i with consequent changes in blood volume ν_i and deoxyhemoglobin content q_i.

[2]Caveat: The state depends on the experimental design thus intrinsic coupling is unique and chracterize each experiment.

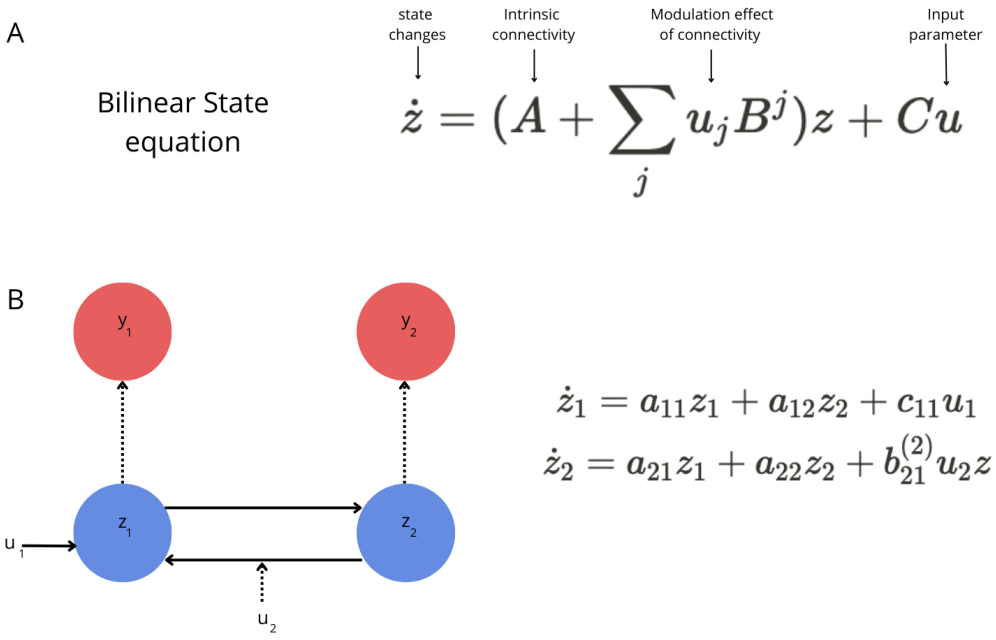

Figure 3.1: (A) The bilinear state equation of DCM where the modulation of connectivity can also be considered as induced connectivity . (B) An example of a DCM describing the dynamic of a system of visual areas , consisting in two regions each described by a state variable (z_1, z_2). Black arrow represent the directional connection between neural states (blue color) whereas dotted arrow represent transformation from neural state into BOLD signal(red colour) also referred as hemodynamic observations.

$$\begin{aligned} \dot{s}_i &= z_i - \kappa_i s_i - \gamma_i(f_i - 1) \\ \dot{f}_i &= s_i \\ \tau_i \dot{\nu}_i &= f_i - \nu_i^{\frac{1}{\alpha}} \\ \tau_i \dot{q}_i &= \frac{f_i E(f_i, \rho_i)}{\rho_i} - \frac{\nu_i^{\frac{1}{\alpha}} q_i}{\nu_i} \end{aligned} \tag{3.5}$$

where throughout the Grubb's exponent [17] we can exert a modulation effect on the outflow as $f_{out}(\nu) = \nu^{\frac{1}{\alpha}}$ and the oxygen extraction is in function of the flow $E(f, \rho) = 1 - (1 - \rho)^{1/f}$[3].
The BOLD signal is taken to be a static nonlinear function of volume and deoxyhe-

[3] ρ is the resting oxygen extraction fraction

moglobin:

$$
\begin{aligned}
y_i &= g(q_i, \nu_i) = V_0(k_1(1-q_i) + k_2\left(1 - \frac{q_i}{\nu_i}\right) + k_3(1-\nu_i)) \\
k_1 &= 7\rho_i \\
k_2 &= 2 \\
k_3 &= 2\rho_i - 0.2
\end{aligned}
\tag{3.6}
$$

where $V_0 = 0.02$ is resting blood volume fraction. The main prior of biophysical parameters $\theta^h = \{\kappa, \gamma, \tau, \alpha, \rho\}$ commonly used are represented in the following table and a block diagram of the hemodynamic model is shown in Fig. (3.2)

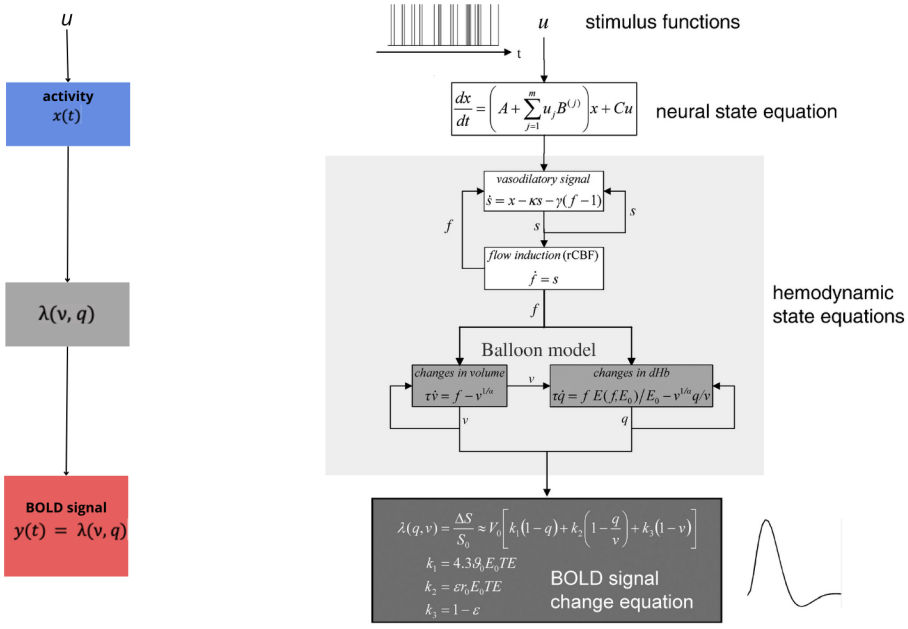

Figure 3.2: This is an adaptation fom *Stephan et al.,2007c* and where use z referring to the activity instead of x. The neuronal activity evoke a vasodilatory and activity dependent signal s which increase blood flow f. Blood flow then causes changes in volume and deoxyhemoglobin(v and q). In [18] the model has six state variables : the rate constant of the vasodilatory signal decay (κ), the rate constant for auto-regulatory feedback by blood flow (γ), transit time (τ), Grubb's vessel stiffness exponent(α), capillary resting net oxygen extraction (E_0), and ratio of intra-extravascular BOLD signal(ϵ). E is the oxygen extraction function. This figure graphically represent the transition from neuronal states to hemodynamic response.

Parameter	Description	Prior Mean η_θ	Prior Variance C_θ
κ	Rate of signal decay	0.65 s	0.015
τ	Hemodynamic transit time	0.98 s	0.0568
ρ	Resting oxygen extraction fration	0.34	0.0024
γ	Rate of flow-dependent elimination	0.41 s	0.002
α	Grubb's exponent	0.32	0.0015

Table 3.1: Priors on biophysical parameters

3.1.3 Estimates

The parameters $\theta = \{\theta^c, \theta^h\}$[4] are estimated from the measured BOLD data following a posterior density analysis under a Gaussian assumption.[15] Briefly, starting from a full forward model that is specified by (3.2) and (3.5)(3.6) :

$$\dot{x} = f(x, u, \theta) \tag{3.7a}$$
$$y = \lambda(x) \tag{3.7b}$$

where $\dot{x} = f(x, u, \theta)$ is the state equation , $x = \{z, s, f, \nu, q\}$ is the combination of neural and hemodynamic states, u the model inputs and θ the parameter set described shortly before. For different combination of parameter θ and inputs u the equation (3.7a) can be integrated and passed through (3.6) to obtain a predicted response $h(u, \theta)$. A detailed description on how to compute $h(u, \theta)$ can be found in *Friston, 2002, Section 3.4* [66] or alternately in *Friston et al., 2003, Section 2.2* [15]. Moreover the forward model can be refined by adding error and confounding or nuisance variables $X(t)$ obtaining $y = h(u, \theta) + X\beta + \epsilon$ where β are the unknown coefficients of the confounds.
Following [66] and thus using Laplace smoothing[74] we end up with :

$$\begin{aligned} y - h(u, \eta_{\theta|y}) \approx J\Delta\theta + X\beta + \epsilon = [J, X] \begin{bmatrix} \Delta\theta \\ \beta \end{bmatrix} + \epsilon \\ \Delta\theta = \theta - \eta_{\theta|y} \\ J = \frac{\partial h(u, \eta_{\theta|y})}{\partial \theta} \end{aligned} \tag{3.8}$$

This local approximation enters subsequently an estimation algorithm based on *Expectation maximization (EM)* [11][66].Once the parameters have been estimated , the posterior distributions [5] of the parameters estimates can be used to test the connection strength. Usually the hypothesis to be tested concern changes in coupling due to experimental environment variations or external stimuli.[18]

[4] Respectively the neural and hemodynamic parameters

[5] Due to Laplace approximation the posterior distribution will be defined by maximum a posteriori (MAP) estimate and their posterior covariance

3.2 Sparse Dynamic Causal Modelling

Since its introduction almost two decades ago, Dynamic Causal Modelling (DCM) has gone through refinement with numerous discoveries. These have helped to shed light on and delve deeper into the inner complexity of the human brain. The non linear equation (3.1) was modified to embody an updated knowledge on biophysical parameters and to account for MRI acquisition parameter such as *echo time* [18] and *slice timing*[105][104]. Further extended model included excitatory and inhibitory subpopulations in each region allowind a detailed description of intrinsic connectivity (between subpopulations) within a region, where a positive constraint was set to reflect that extrinsic(inter-regional) connections of cortical areas are purely excitatory.[2] Other approaches took into consideration the limitations of the biliniar model(3.2) :

1. the neuronal origin of the modulatory influence is not specified
2. may be not the appropriate framwork to model. fast changing in EC , which are mediated by non linear effect at the level of single neuron. [65]

thus proposing a solution that considered nonlinear interaction among synaptic inputs where the *effective strength* of a connection between two regions is modulated by activity in a third region.[58]
One of the latest approches ,proposed by *Prando et al.,2020*[49] , extended the previous resting-state DCM procedure (*Friston et al.,2014*[67]) by overcoming the principle that the procedure would work only with a restricted set of nodes.

The *Sparce Dynamic causal modelling* ,in fact, gives a wider range on information by estimating whole-brain effective connectivity form resting-state fMRI data. Having as reference the stochastic DCM proposed in *Friston et al,2014*[67] it has been introduced a a discretization of the non-linear model and a statistical linearization of the HRF.
Considering the general mathematical expression of the DCM model

$$\begin{aligned} \dot{x}(t) &= f(x(t), u(t), \theta_f) + \nu(t) \\ y(t) &= h(x(t), \theta_h) + e(t) \qquad\qquad e(t) \sim \mathcal{N}(0, R) \end{aligned} \tag{3.9}$$

where $\dot{x}(t)$ describes the coupling among neuronal populations, $h(x(t), \theta_h)$ a dynamic map from neuronal activity to measured BOLD signal $y(t)$, $\nu(t)$ is a stochastic term representing intrinsic brain fluctuations , $e(t)$ account for observation noise with covariance matrix R and θ_f describe the model at neural level whereas θ_h are biophysical parameters defining the hemodynamic response. Under the assumption that external stimuli are absent[6], $u(t) = 0$ and applying on (3.9) the discretization and the linearization cited before , we end up with :

$$\begin{cases} \mathbf{x}(k+1) = \mathbf{A}\mathbf{x}(k) + \mathbf{w}(k) \\ \quad y(k) = \mathbf{H}\mathbf{x}(k) + e(k) \end{cases} \tag{3.10}$$

[6]The random fluctuations $\nu(t)$ remain the only term that drives the neural activity thus the non-linear function in (3.9) becomes linear $\dot{x} = Ax(t) + \nu(t)$

where **A** refers to the EC matrix, $\mathbf{w}(k)$ represent wite gaussian noise associated with endogenous fluctuations with variance Q [54] and $e(k)$ describes the measurement error trough a white gaussian variable with variance R.[49]
The matrices **A** and **H** are defined as follow:

$$\mathbf{A} = \begin{bmatrix} e^{AT_R} & 0 \\ \mathbf{I}_{n(s-1)} & 0 \end{bmatrix} \tag{3.11}$$

$$\mathbf{H} = \begin{bmatrix} h_{1,0} & 0 & \dots & 0 & h_{1,1} & 0 & \dots & 0 & \dots & h_{1,s-1} & 0 & \dots & 0 \\ 0 & h_{2,0} & \ddots & \vdots & 0 & h_{2,1} & \ddots & \vdots & \dots & 0 & h_{2,s-1} & \ddots & \vdots \\ \vdots & \ddots & \ddots & 0 & \vdots & \ddots & \ddots & 0 & \dots & \vdots & \ddots & \ddots & 0 \\ 0 & \dots & 0 & h_{n,0} & 0 & \dots & 0 & h_{n,1} & \dots & 0 & \dots & 0 & h_{n,s-1} \end{bmatrix}$$

where **A**, **H** are components of the parameter vector $\theta = \{\mathbf{A}, \sigma, h_1, \dots, h_n, \lambda_1, \dots, \lambda_n\}$ estimated following the EM algorithm explained in *Prando et al.,2020* (Section 2.3)[49].
In brief, given $\{y(k)\}_{k=1}^{N}$ measure of the BOLD signal we want to find θ and γ that maximize the marginal posterior

$$p_\gamma(\theta|Y) = \int p_\gamma(\mathbf{X}, \theta|Y) d\mathbf{X} \tag{3.12}$$

where $Y = [y^T(1), \dots, y^T(N)]^T$ and $\mathbf{X} = [x^T(0), \dots, x^T(N)]^T$ as measurement and latent variables respectively.
However, due to computational challenges of this high-dimensional integral, a tractable lower bound of the likelihood is exploited.
The prior $p_\gamma(\theta)$ is specified, assuming uninformative priors for some parameters and employing a sparsity-inducing prior for the connectivity matrix A based on Sparse Bayesian Learning (SBL). The SBL perspective allows for the automatic selection of a sparsity pattern in the estimated effective connectivity matrix, avoiding combinatorial search over candidate network structures.
The Maximum A Posteriori (MAP) estimate is obtained using an Expectation-Maximization (EM) procedure. The EM algorithm iteratively optimizes a lower bound of the log-posterior, incorporating a priori information on θ. The procedure involves maximizing the lower bound with respect to an arbitrary distribution and θ. The computational complexity of each iteration is $O((ns)^3)$, primarily due to matrix inversions in the Rauch-Tung-Striebel smoother. The EM algorithm alternates between the RTS smoother and the maximization of the lower bound to update θ. Hyperparameters $\gamma_{i\,i=1}^{n^2}$ are also updated at each iteration, crucial for inducing sparsity on A.
The non-convexity of the problem is addressed, emphasizing the importance of proper initialization ($\theta(0)$ and $\gamma_{i\,i=1}^{n^2}$). Experimental investigations highlight the critical role of the effective connectivity matrix A in the initialization process, providing insights reported in the Appendix B (Algorithm 1)[49]. The overall computational cost scales as $O((ns)^{3N})$ for N iterations, and specific details on execution times are provided in **Sections 3.1 and 3.2**[49].

The estimated matrix A is non-symmetric matrix and each row and column represents a specific region of interest. The information about the effective connections between each pair of regions is directed, for example, the weight of the link in position 10,20 (row, column) of the matrix represents the strength of the link that region 20 exerts on region 10. Values in the diagonal give information about the recurrent links of each region.
The matrix A can be also thought, under a graph theory representation , as an adjances matrix enabling us to retrieve *nodes*(region of interest like brain network) and the respective edges.

Chapter 4

Materials and Methods

This section will provide a complete description of the rs-fMRI as well as [^{18}F]FDG PET dataset and acquisition settings. It also presents the subject's demographical as well as the neoplasm data and the chosen reference atlas.

4.1 Healthy and Oncology datasets

Healthy Dataset
Healthy subjects were recruited to match the oncology patients, 42 subject were drafted (19M, 23F) with mean age of 58.2 (age: 58.2 ± 14.5)

Oncology dataset
Oncology subjects were recruited resulting in 42 (19M, 24M) patients with different brain neoplasm types, with mean age 58.8 (age: 58.8 ± 14.9). Additional information about tumor's grade, histology and location are provided in table (Tab.4.1).

Tumor histology	
Astrocytoma	2
Diffuse astrocytoma	1
Glioblastoma	28
Gliosarcoma	1
Glioneural neoplasm	2
Oligodendroglioma	1
Other	8
Tumor grade	
I	1
II	7
III	4
IV	28
n.a.	3
Tumor site	
Left	24
Right	15
Bilateral	4

Table 4.1: Tumor's grade, histology and site among oncology dataset

4.2 Atlas

The choice for the reference atlas relapsed on a homotopic variant oh the gwMRF local-global parcellation model developed by *Yan et al.[119]*, where each parcel has a spatial counterpart on the other hemisphere. The resulting parcels are homogeneous in both resting and task states across datasets from diverse scanners, acquisition protocols, pre-processing and demographics. Additionally , the homotopic local-global parcellations replicate known homotopic and lateralization properties of the cerebral cortex.

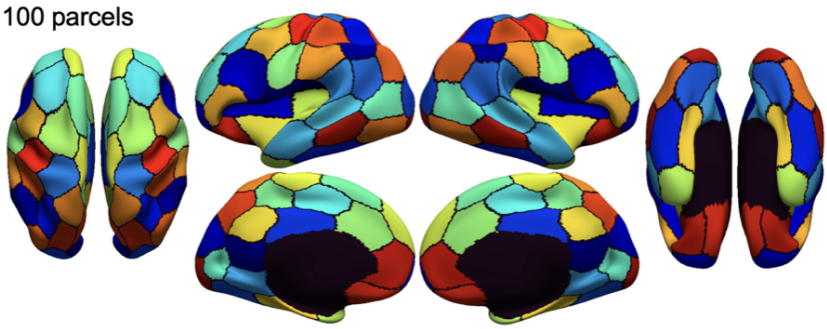

Figure 4.1: Homotopic parcellation from rs-FC . Cerebral cortex parcellations with 100 parcels based on the full GSP dataset of 1479 subjects. Homotopic parcels have identical colors. (*Yan et al.,2023*)[119]

For computational complexity reasons it has been necessary to reduce the number of nodes considered as input before applying sparse DCM by utilizing the framework proposed in *Ryali et al.*[109], termed *consensus clustering*, which is based on a combination of a base K-means clustering(KC) and hierarchical clustering(HC). By applying this framework it has been possible to retrieve the optimal number of stable cluster in rs-fMRI data. It has also to be stated that subcortical parcels were kept unchanged and with respect of *Ryali et al,* the modified silhouette was used as objective criteria to determine the number of cluster. Clustering was only performed on ROIS that were functionally homogeneous and spatially contiguous in order to preserve the spatial consistency of the hemodynamic properties.
The correspondence between the original Brain areas and the clusterized functional network are shown in table (Tabl.4.2) whereas the resulting atlas is shown in figure (Fig.4.2)
From here on we would refer at the clusterized Yan atlas as *c-Yan*.

Figure 4.2: Clusterize version of Yan homotopic atals . Cerebral cortex parcellations with 100 parcels based on the full GSP dataset of 1479 subjects were reduced by consensus clustering[109] into 74 cortical ROIs.(See Tabl.4.2)

ID	Network	Areas
1	Default	FPole
2	Default	IPL 1
3	Default	IPL 2
4	Default	PCC, RSC
5	Default	PFCd 1, PFCm
6	Default	PFCd 2
7	Default	PFCd 3
8	Default	PFCv 1
9	Default	PFCv 2
10	Default	Temp 1
11	Default	Temp 2
12	Default	Temp 3
13	Cont	IPS
14	Cont	PCC
15	Cont	PFCl
16	Cont	PrCv
17	Cont	pCun
18	Limbic	OFC
19	Limbic	PHC
20	Limbic	Temp, TempPole
21	SalVentAttn	FrMed
22	SalVentAttn	Ins 1/2
23	SalVentAttn	PostC
24	SalVentAttn	SPL
25	DorsAttn	IPS, SPL 2
26	DorsAttn	PostC
27	DorsAttn	PrC, PrCd
28	DorsAttn	SPL 1
29	DorsAttn	TempOcc
30	SomMot	1/3/4
31	SomMot	2
32	SomMot	5
33	SomMot	6
34	SomMot	Ins
35	SomMot	ParOper
36	Vis	1/2/4
37	Vis	3/5/6/7
75	Subcortical	Thalamus
76	Subcortical	Caudate
77	Subcortical	Putamen
78	Subcortical	Pallidum
79	Subcortical	Cerebellum
80	Subcortical	Hippocampal

ID	Network	Areas
38	Default	IPL 1
39	Default	IPL 2
40	Default	PCC, RSC
41	Default	PFCd 1,PFCm
42	Default	PFCv 1
43	Default	Temp 1
44	Default	Temp 2
45	Cont	FPole
46	Cont	IPS
47	Cont	PCC
48	Cont	PFCd
49	Cont	PFCl
50	Cont	PFCv
51	Cont	PrCv
52	Cont	pCun
53	Limbic	OFC
54	Limbic	Temp, TempPole
55	SalVentAttn	FrMed
56	SalVentAttn	Ins 1/2
57	SalVentAttn	PFCd
58	SalVentAttn	ParOper
59	SalVentAttn	PostC
60	SalVentAttn	SPL
61	DorsAttn	IPS, SPL 2
62	DorsAttn	PrC, PrCd
63	DorsAttn	SPL 1
64	DorsAttn	TempOcc
65	SomMot	1/3/4
66	SomMot	2
67	SomMot	5
68	SomMot	6
69	SomMot	Ins
70	SomMot	PostC
71	SomMot	Temp
72	Vis	1/2/4
73	Vis	3/5/6/7
74	Vis	PHC
81	Subcortical	Thalamus
82	Subcortical	Caudate
83	Subcortical	Putamen
84	Subcortical	Pallidum
85	Subcortical	Hippocampal
86	Subcortical	Cerebellum

Table 4.2: Atlas clustering (left and right hemisphere)
These are the results of a consensus clustering algorithm applied to the 100-area parecellation (7-networks) of [119] and AAL2 subcortical parcellation

4.3 Healthy subjects

For each subject in the dataset rsfMRI and [^{18}F]FDG scans were performed. All data were processed according to the procedure explained in *Volpi et al.,2023*[113].

4.3.1 fMRI acquisition protocol

Structural images were acquired using a 3D sagittal T1-weighted magnetization-prepared 180° radio-frequency pulses and rapid gradient-echo (MPRAGE) multi-echo sequence (TE = 1.81, 3.6 , 5.39, 7.18 ms, TR = 2,500 ms, TI = 1,000 ms, 0.8×0.8×0.8-mm voxels). The final T1w image was obtained as the average of the first two echoes.[62] $T2^*$ gradient-echo echo planar imaging (GE-EPI) data were acquired (TR/TE=800/33 ms, flip angle 52°, voxel size 2.4×2.4×2.4 mm, MB 6, 375 volumes for total scan time of 5 min), together with two spin-echo (SE) acquisitions (TR/TE=6000/60 ms, flip angle 90°) with opposite phase encoding directions (AP, PA), often used for distortion correction. All data types were acquired on a Siemens Magnetom Prisma^{fit} scanner.

4.3.2 fMRI pre-processing

The fMRI data were processed in a similar way to the Human Connectome Project minimal processing pipeline [62]. The first four volumes were discarded to avoid non equilibrium magnetization effects. The remaining volumes were corrected for slice timing differences and magnetic field distortion and realigned to the median volume. A template EPI volume was obtain from realigned fMRI data and used to estimate an affine tranform employed to map main tissue segmentations from T1w image to the EPI space.
Nuisance signal and the first 5 temporal principal components obtained after PCA of WM and CSF EPI signals, were regressed out from all brain voxels in native EPI space. Moreover BOLD signal was cleaned from motion atrifacts with an ICA-based approach (ICA AROMA [92]) and high-pass filtered(cut-off 0.008 HZ).
Finally, pre-processed rs-fMRI were obtained within each ROI from the *c-Yan* atlas (See Tabl.4.2), which had been linearly mapped from T1w to rs-fMRI space by averaging over voxels within the T1w GM segmentation (Probability >0.8 of belonging to GM).

4.3.3 [^{18}F]FDG-PET acquisition protocol

[^{18}F]FDG scans were performed on a Siemens model 962 ECAT EXACT HR + PET scanner (Siemens/CTI) , as previously described [107][44], after i.v. bolus injection of 5.1 ± 0.3 mCi (187.7 ± 12.1 MBq) of [^{18}F]FDG. Dynamic acquisition of PET emission data continued for 60 min. Participant head movements during scanning were restricted by a thermoplastic mask. All PET images were acquired in the eyes-closed waking state. No specific instructions were given during scanning other than to remain awake.

[^{18}F]FDG PET data Reconstruction PET data were reconstructed via filtered back-projection (ramp filter, 5 mm FWHM) as 128x128x63 matrices. The reconstruction grid consisted of 52 frames of increase duration (24 x 5 s frames, 9 x 20 s frames, 10 x 1 min frames, and 9 x 5 min frames). To address attenuation correction, participant-specific transmission scans were utilized for performing the necessary corrections.

4.3.4 [^{18}F]FDG-PET pre-processing

The dynamic ^{18}F]FDG data were motion corrected using the FSL's *mcflirt* algorithm.[80] For each subject in the dataset a static [^{18}F]FDG image was computed by summing the motion-corrected late [^{18}F]FDG frames acquired between 40 and 60 minutes. The static image was linearly registered to T1w space using FSL's flirt algorithm [80] and the *c-Yan* parcellations and the individual GM and WM tissues segmentations were mapped from T1w to PET space. Finally [^{18}F]FDG static PET image was normalized to SUVR by dividing the value of ech voxel by the average uptake of [^{18}F]FDG in the whole brain.

4.4 Oncological subjects

For each subject in the dataset were performed rsfMRI and [^{18}F]FDG scans. fMRI data were processed according to *Pagnin,2022* (Section 6.2)[90] .

4.4.1 fMRI acquisition protocol

Data were acquired on a 3 T Siemens Biograph mMR scanner equipped with a 16-channel head–neck coil. Anatomical imaging included T1-weighted (T1w) 3D magnetization-prepared rapid acquisition gradient-echo (TR = 2400 ms, TE = 3.24 ms, TI = 1000 ms, FA = 8°, FOV = 256 × 256 mm, voxel size = 1 mm × 1 mm × 1 mm) images acquired both before and after contrast agent injection, a 3D T2-weighted image (TR = 3200 ms, TE = 535 ms, FOV = 256 × 256 mm, voxel size = 1 mm × 1 mm × 1 mm), a 3D fluid attenuation inversion recovery (TR = 5000 ms, TE = 284 ms, TI = 1800 ms, FOV = 256 × 256 mm, voxel size = 1 mm × 1 mm × 1 mm) image. In addition, functional imaging comprised rs-fMRI EPI scans (TR = 1260 ms, TE = 30 ms, FA = 68°, FOV = 204 × 204 mm, voxel size = 3 mm × 3 mm × 3 mm, volumes = 750, MBAccFactor = 2, iPAT = 0, phase encoding direction antero-posterior) and two spin echo-EPI acquisitions with 41 reverse phase encoding (TR = 4200 ms, TE = 70 ms, FOV = 204 × 204 mm, voxel size = 3 mm × 3 mm × 3 mm, MBAccFactor = 1) for EPI distortion correction purposes.

4.4.2 fMRI pre-processing

The rs-fMRI data pre-processing pipeline is composed by: a slice timing procedure, a readout distortion correction(FSL's TOPUP), a realignment of volumes according to *mcflirt* algorithm [80], a non-linear mapping to the symmetric MNI152 atlas

exploiting the subject-specific T1w (via FSL's boundary based registration) and high pass filtering (cut-off frequency: 0.008 Hz), a manual identification and out-regression of the ICs related to broad head movement artifacts. Moreover the first 5 principal components related to CSF and WM signal were regressed out from rs-fMRI time series as well as head-motion parameters and the associated derivatives. To quantify subject -specific head motion during the scan , it has been computed a frame-wise displacement.
The rs-fMRI signals has been subsequently projected onto the atlas described in section (4.2) and despiked in order to mitigate deterioration in accuracy of volume registration and computational performances .(cite 41) Despiking was performed using an average approach on the function *icatb_ despike_ tc* , which is contained in Group ICA Toolbox (https://trendscenter.org/software/).
Timeseries were then further temporally filtered to reduce noise outside frequencies of interest using a band-pass filter(0.0078-0.2 Hz) obtained as combination of high and low-pass Butterworth filters.
More details about thereof steps and their reasons of choice can be found in *Pagnin,2022* (Section 6.2)[90]
Therefore, from the initial rs-fMRI data registered in the *Yan* atlas reference space, we would obtain data projected in a reduced space of 74 cortical regions.

4.4.3 [^{18}F]FDG-PET acquisition protocol

[^{18}F]FDG PET and structural MRI images were acquired for patients. Hence Glioma patients underwent simultaneous PET/MR acquisitions on a Siemens 3T Biograph mMR scanner (Siemens Medical Solutions USA, Inc.). Dynamic PET acquisitions of 60 min duration were performed following an i.v. bolus injection of 203 $\pm$ 40 MBq. Images were then reconstructed as matrices of size 256x256x127 with a voxel size of 2.8x2.8x2.0 mm using the OSEM algorithm starting from list-mode data. The reconstruction grid comprised 39 frames with increasing duration: 10 frames of 6 s, 8 frames of 15 s, 9 frames of 60 s and 12 frames of 240 s.

4.4.4 [^{18}F]FDG-PET pre-processing

The dynamic [^{18}F]FDG data were motion corrected using the FSL's *mcflirt* algorithm.[80] For each subject in the dataset a static [^{18}F]FDG image was computed by summing the motion-corrected late [^{18}F]FDG frames acquired between 40 and 60 minutes. The static image was linearly registered to T1w space using FSL's *flirt*[80] algorithm and the tumor mask (TM) and lesion mask (TM+E) as well as *c-Yan* parcellations and the individual GM and WM tissue segmentations were mapped from T1w to PET space. Then the static ^{18}F]FDG PET image was normalized dividing by the average uptake of ^{18}F]FDG in the WM SPM map (probability >0.95 of belongin to WM) resulting in SUVR . It has to be noted that the cerebellum was chosen as reference region given the low incidence of gliomas (4.5% of all gliomas).

4.5 MC estimate

A segmented version of Yan atlas was obtained masking the atlas with GM mask(probability of belonging to GM>0.5) corresponding to 74 cortical regions and with a notCSF mask(probability of not belonging to CSF >0.95) correspondig to 12 subcortical regions. Region of interest (ROI)-level [^{18}F]FDG PET time-activity curves (TACs) were derived from the Yan segmented atlas by averaging voxel values within each parcel. Subsequently, the five-second frames were temporally filtered by averaging them in triplets, employing a subsampling approach for the initial 24 frames with a 3x3 averaging. Finally, all TACs were interpolated onto a uniform virtual time grid.
The core analysis revolves around the calculation of Euclidian similarty matrices between pairs of brain regions. This metric captures reseamblance in the temporal profiles of metabolic activity, offering a quantitative measure of within-individual Metabolic Connectivity.
Euclidean similarity it is based on the Euclidean distance d_{x_1,x_2} between each pair of TACs $x_{i,1}$ and $x_{i,2}$:

$$d_{x_1,x_2} = \sqrt{\sum_{i=1}^{T}(x_{i,1} - x_{i,2})^2} \tag{4.1}$$

where T is the number of time points. From $d_{x1,x2}$ then the *Euclidean similarity* is derived aa 1 minums the normalized $d_{x1,x2}$ (e.g. divided by the maximum distance among pairs of TACs).

4.6 SUVR estimate

Applying the procedure outlined in Section 4.5, masks delineating regions of interest (ROIs) were created. Standardized Uptake Value (SUV) calculations were performed on static PET images (frames acquired between 40-60 minutes) by dividing voxel values within the static PET by the ratio of the known injected dose to the subject's weight. Subsequently, SUV ratio (SUVR) maps were generated from SUV values, utilizing the average uptake of [^{18}F]FDG in the white matter (WM) according to the SPM map (probability > 0.95 of belonging to WM).

4.7 sparse DCM algorithm inizialization

4.7.1 DCM Noise variance setup

A required step to apply sparse DCM is to set a critical parameter teremd noise variance , as elucidated in section(riferimento alla sezione). This parameter corresponds to the variance of the measurement noise, embedded in the R matrix within the sDCM framework. Determining the optimal value involves an iterative process where different weights for the R matrix (expressed as a fraction of the sample variance of the input BOLD signal) are tested. The aim is to strike a balance between the empirical-simulated Functional Connectivity (eFC-sFC factor) and the Kolmogorov-Smirnov (KS) distance, following the methodology outlined in *Deco et*

al.2017[47].
The eFC-sFC factor is computed by considering the ground static Functional Connectivity (FC) matrix. This matrix represents correlations between pairs of BOLD signals extracted from brain areas over the entire time window of acquisition, with correlation values ranging from -1 to +1. The eFC-sFC correlation factor is then determined as the Pearson correlation between the upper triangular part of the empirical FC matrix, derived from observed BOLD signals, and the simulated FC matrix obtained through sDCM estimation The simulation involves generating a time response of a dynamic system to arbitrary inputs, based on system matrices computed through the sparse estimation algorithm [49].
According to *Deco et al, 2017* the Dynamic Functional Connectivity (FCD) matrix is computed using a sliding window approach. Then , the resulting FCD matrix , with entries defined by Pearson correlation between corresponding FC matrices is used to compare upper trisngular elements across subject and sessions.The Kolmogorov-Smirnov (KS) distance is then computed, quantifying the maximal difference between the cumulative distribution functions of the empirical and simulated data as shown in figure(4.3) In summary, the objective of determining the

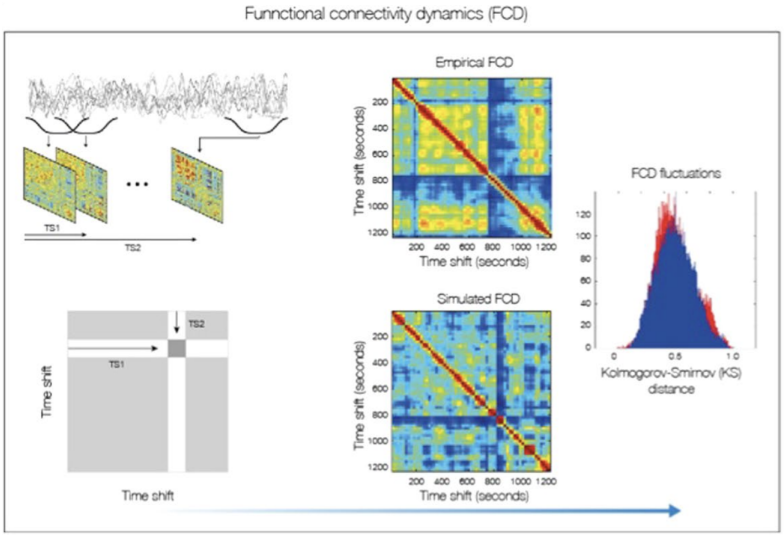

Figure 4.3: Methods for measuring fit between simulated and empirical data. For comparing the FCD statistics, we collected the upper triangular elements of the matrices (over all participants or sessions) and compared the simulated and empirical distribution by means of the Kolmogorov-Smirnov distance between them. The Kolmogorov–Smirnov distance quantifies the maximal difference between the cumulative distribution functions of the two samples. (*Deco et al.,2017*)[47]

optimal noise variance is to find a value that maximizes the correlation between empirical and simulated FC while minimizing the KS distance. This subject-specific procedure results in the selection of a value that performs well across all subjects.

4.8 Metabolic and EC derived metrics comparison

After having obtained both an EC and MC estimate for each subject in the dataset we would consider three entropy-related metrics namely Σ which is a symmetric matrix that quantifies the dissipative flow, S which is an antisymmetric matrix that measure the solenoidal flow and Σ^{-1} which is a precision matrix.

4.8.1 Σ and S matrices

According to *Prando et al.,2020*[49] the intrinsic random brain fluctuation $\nu(t)$ in the DCM model equation remain the only term that drives the neaural activity , thus the non-linear function in (3.9) becomes linear:

$$\dot{x}(t) = Ax(t) + \nu(t) \tag{4.2}$$

where x contains the states of brain regions , A is the EC matrix encoding relationships between brain regions and Σ_ν is the covariance matrix associated to the noise variance estimated in 4.7.1.
In accordance with *Casti et al.,2023*[115] and *Benozzo et al.,2023*[37] , supposing A Hurwitz stable, the A matrix can be decomposed as

$$A = \left(-\frac{1}{2}\Sigma_\nu + S\right)\Sigma^{-1} \tag{4.3}$$

where Σ^{-1} is the inverse matrix of Σ. The Σ matrix also can be seen as a measure of functional strength between brain regions and can be computed as the solution of the Lyapunov equation:

$$A\Sigma + \Sigma A^T + \Sigma_\nu = 0. \tag{4.4}$$

The S matrix can be consequently computed as $S = \frac{1}{2}(A\Sigma - \Sigma A^T)$.(See *Proof* Thm.1 [115])

4.8.2 Correlations

For each subject all three matrics explained in 4.8.1 were computed for EC subject-specific data and then considered along with SUVR and MC subject-specific data following 2 main approaches:

1. The strength of Σ, Σ^{-1} , S and MC were obtained by summing over each matrix column resulting in four row vectors with dimension of 1x86 (*1 x number of c-Yan parcels*). All vectors were then merged into matrices , respectively Σ_{str}, Σ^{-1}_{str} , S_{str} and MC_{str} with dimension (*number of subjects x number of c-Yan parcels*).

2. For each Σ, Σ^{-1} , S and MC matrices were extracted their upper triangular matrices, resulting in a vector of dimension 3655x1 (*number of element in the strictly upper triangular matrix* where the number of upper element can be computed as $\sum_{k=1}^{n-1}(n-k)$ with $n = 86$ number of *c-Yan parcels*.

For both approaches *Spearman correlation* was computed between coupled metrics as follow : Σ-MC, S-MC, Σ-$SUVR$, S-$SUVR$,Σ^{-1}-MC and Σ^{-1}-$SUVR$.
Subsequently each vector containing correlation coefficients of the coupled metrics was corrected for multi-comparison type 1 error(False positive) using the *multicmp* function (https://www.mathworks.com/matlabcentral/fileexchange/61659-multicmp)[19] with significance threshold set to $\alpha = 0.05$.
Non significant values of correlation were finally set to zero.
Moreover, the complete process described above was repeated considering absolute values of the metrics (e.g. for MC_{str} the sum over columns of its element's absolute values) to check if it would affect the correlation coefficients.

4.9 Oncological and HC comparison

Wilcoxon Rank sum test
Correlations were separately calculated for the Healthy and Oncology datasets, and the resulting vectors were processed to remove zero values. Resulting vectors were tested for normality using *Lilliefor test* with a significance level 5%($\alpha = 0.05$).The test was chosen given the fact that it adjust for estimation of parameters from the sample consequently being more accurate when dealing with small sample size.
Only for one correlation vector the test couldn't reject the null hypothesis , however being composed by just two data points, the interpretation of the test was unsure. For this reason all vector are supposed non normally distributed. In addiction to that the use of paired t-test is not recommended, given the fact that the sample sizes were small for each cleaned correlation vector.[88]
Therefore, significant independent correlation's vectors between healthy and oncology subjects were compared for similarity in median with *Wilcoxon Rank sum test*[26] where significant differences in median were selected for $p_{value} < 0$.

4.10 Network influence assessment

An evaluation on network influence on the relationship between metrics were carried out in the healthy dataset between : $MC - \Sigma^{-1}$, $SUVR - \Sigma^{-1}_{str}$, $|S|_{str} - SUVR$ and $S - MC$.

Sorting by network
Single subject matrices MC, Σ^{-1} and S with dimension 86x86 (*number of c-Yan parcels x number of c-Yan parcels*) and $SUVR$, $|S|_{str}$, Σ^{-1}_{str}vectors with dimension 1x86 (*1 x number of c-Yan parcels*) were sorted by functional network according to table (Tab.4.2), hence e.g. for vector $|S|_{str}$ the first 74 entries would represent the left and right hemisphere cortical *c-Yan* parcels and the last 12 entries the left and right hemisphere subcortical *c-Yan* parcels.

In particular, for MC, Σ^{-1} and S matrices the extraction and consequent rearrangement of functional network was carried out as follow:

1. one vector $\hat{v} = [left, right]$ (left:left hemisphere, right:right hemisphere) was initialized for each functional network, containing the cluster's indices corresponding for that network.(See Tabl. 4.2)

2. an encoding block diagonal matrix was constructed where each square diagonal block represented intra-network ROI . Each diagonal block was a square matrix of dimension kxk (k=length of $\hat{v}$) containing only one entries multiplied for a scalar value such that:

$$a \times \begin{bmatrix} 1 & 1 & 1 \\ 1 & 1 & 1 \\ 1 & 1 & 1 \end{bmatrix}_{kxk}$$

   where $a = 1, \ldots, 13$ represent respectively *Default, Cont, Limbic, SalVanAttn, DorsAttn, SomMat, Vis, Thalamus, Caudate, Putamen, Pallidum, Cerebellum, Hippocampal* networks.

3. upper triangular matrices of dimension 1x3655 were extracted using the same mask for MC, Σ^{-1} and S and the encoding block diagonal matrix.

4. single network data points were extracted from upper triangular MC, Σ^{-1} and S using as reference the indexes in the upper triangular encoding matrix corresponding to the network's a value.

5. finally each network data points collection were merged into a row vector for each metric, obtaining 3 row vectors of dimension 1x434 e.g. $x_{MC} = [n_1, n_2, \ldots, n_{13}]$.

Therefore each final row vector would contain the data points corresponding at the upper triangular matrix ordered by network. It has to be noted that doing so inter-network data were excluded from the analysis.

Influence on correlation assessment
For uniformity in metrics measurement scale $SUVR$, S_{str}, Σ^{-1}_{str}, x_{MC}, x_S and $x_{\Sigma^{-1}}$ were z-scored. Each coupled metric, was then fitted using *fitlm* function and plotted. In addiction, in each plot was superimposed a partial regression leverage plot to help identify influential observations and assess the effect of individual predictor variable on the response variable.

For x_{MC}, x_S and $x_{\Sigma^{-1}}$, given the high number of data points, the average distance between each network and the regression line was considered as metric to evaluate the degree of influence in the correlation. The distance form each data point and the regression line was computed with *point-to-line* [96] function and then distance values within the same network averaged.
Person correlation (significance level 5%) and R^2 were computed among all coupled metrics to evaluate respectively the linearity of the relationship between two metrics and the goodness of the linear fit.

The group-level impact of networks on correlation was assessed through the following

steps: firstly, the average distance between each network and the regression line was computed for each subject, resulting in a vector of dimensions 1x13 (1x*number of functional networks*). Secondly, a matrix M, sized 43x13 (*number of subjects x number of functional networks*), was initialized. Each row in M represented the subject's average distance for each functional network data point from the regression line. Finally, the group-level distance from each network to the regression line was computed by averaging each column of M.
It is important to note that subjects for whom the Pearson correlation exhibited a $p_{value} > 0.05$ were excluded from the M matrix as they did not exhibit a significant linear relationship between fMRI and [^{18}F]FDG PET-derived metrics.

Chapter 5

Results

This chapter will include all the results for sparse DCM setup , Correlation analysis, similarity testing and network influence analysis.
All quantitative measures and figures have been generated with MATLAB2022a (MathWorks, Inc.)

5.1 Choice of Variance

According to the procedure in 4.7.1 a key step before utilizing the sparse DCM algorithm is to set the covariance matrix R as indicates the input observation noise. The choice of the best weight for the noise variance matrix R was performed by computing the empirical-estimated FC (eFC-esFC) correlation(Fig.5.2) and the empirical-estimated FCD Kolmogrov-Smirnov(KS) distance (Fig.5.1).
Starting from a sample group (Tab.5.1) the eFC-esFC factor as well as KS distance have been computed executing the sparse DCM algorithm for nine weights of the noise variance : *1/400, 1/100, 1/50, 1/15, 1/10, 1/5, 1/4, 1/3 and 1/2.*

Subject IDs				
108004	108007	108013	108016	108029
108036	108038	108040	108044	108045

Table 5.1: Subject IDs of the sample group

Subjects corresponding at IDs 108007 and 1080013 didn't reach convergence for none of the weights listed above thus they weren't considered for the choice of the best covariance matrix weights. In the remaining subjects, if convergence weren't reached for a specific weight of noise variance then the correspondent eFC-esFC as well as KS distance were set to zero.

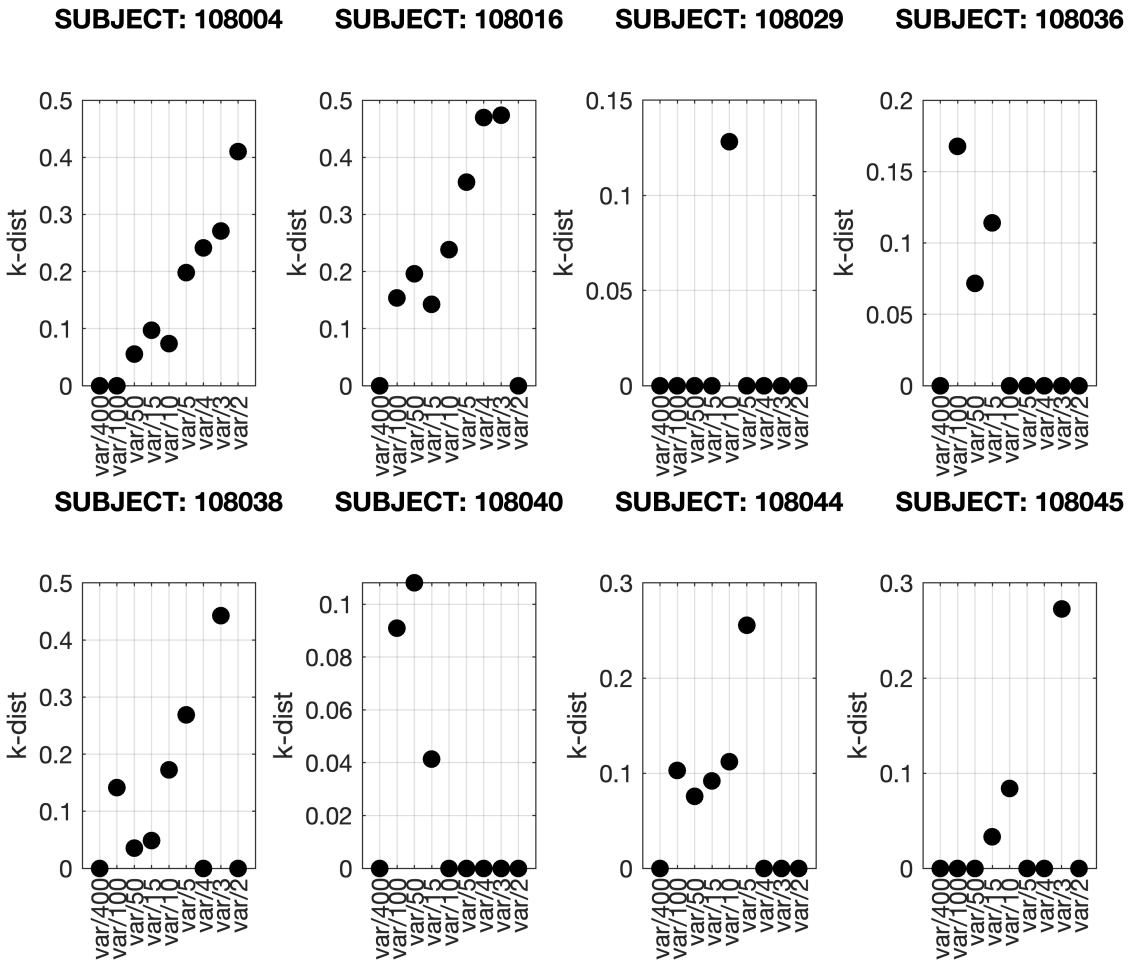

Figure 5.1: Empirical-estimated FCD KS distance. Kolmogorov-Smirnov distance FCD distribution for each of the eight subjects, by calculating the KS distance through the empirical and estimated FCD distribution values. This distance has been computed for all the nine test weight of the noise variance. This factor should be minimized.

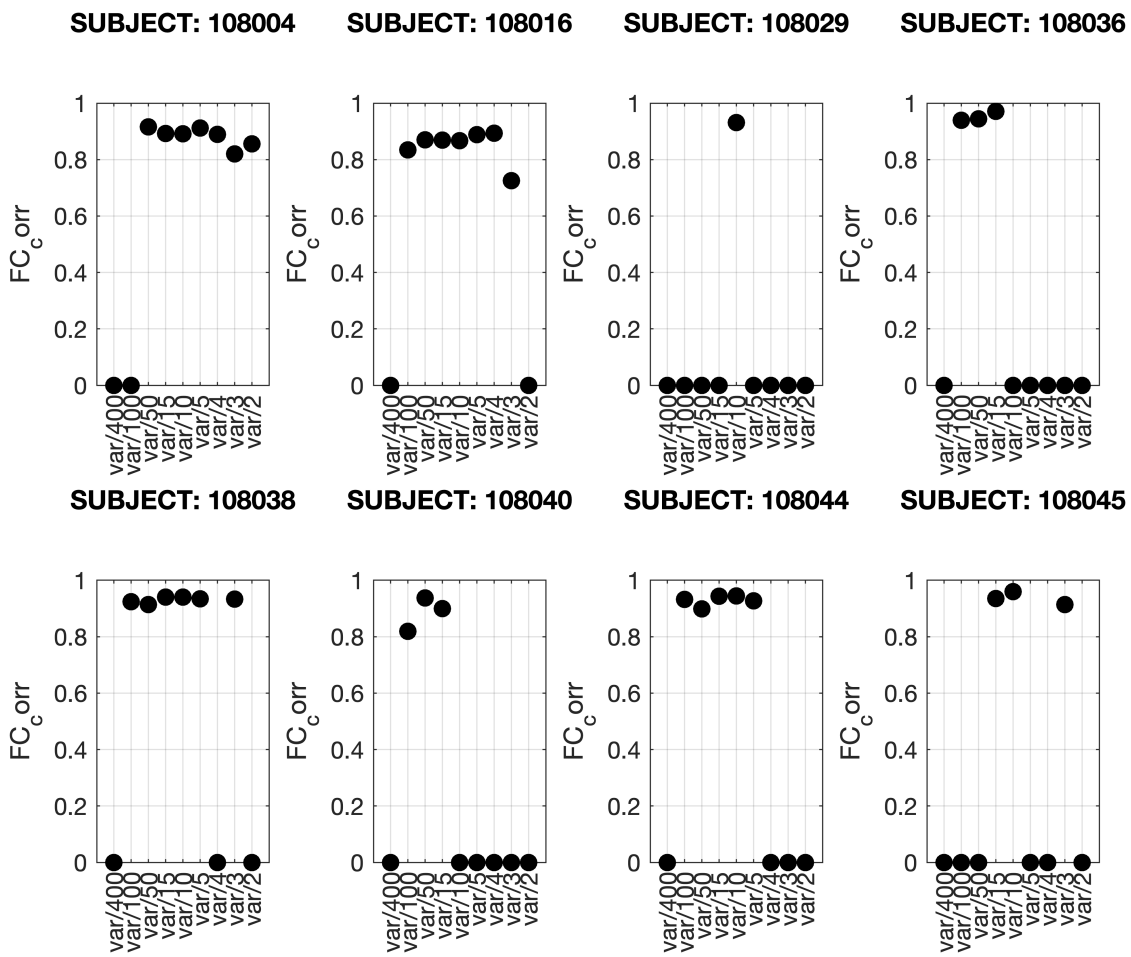

Figure 5.2: Empirical-estimated FC correlation. FC Pearson correlation values for each of the eight subjects, by calculating the Pearson correlation through the empirical FC matrix and the estimated one. The eFC-esFC factor has been computed for nine weights of the noise variance. This factor should be maximized.

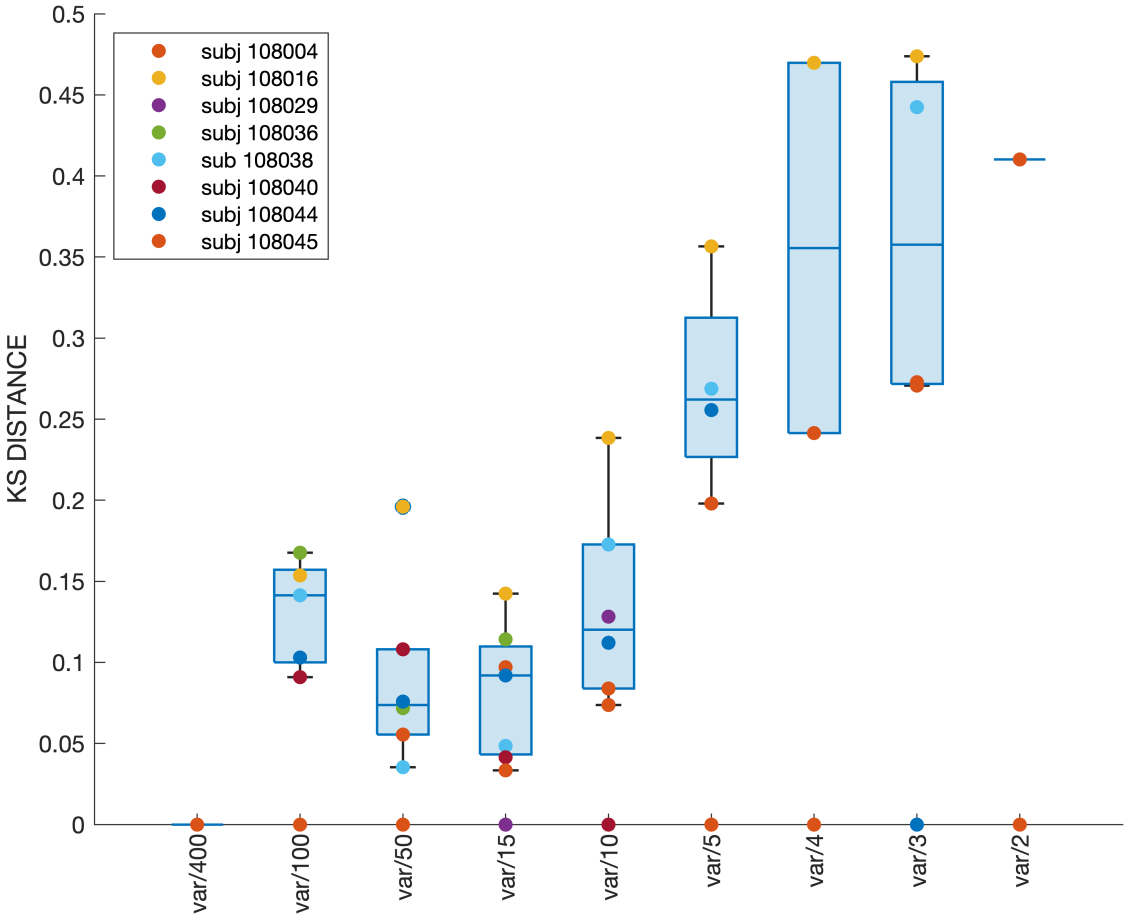

Figure 5.3: Empirical-estimated FCD KS distance through subjects. Visual representation of the KS distance values through subjects for each weight of the noise variance . Mean values across subjects are represented in boxplot by horizontal lines.

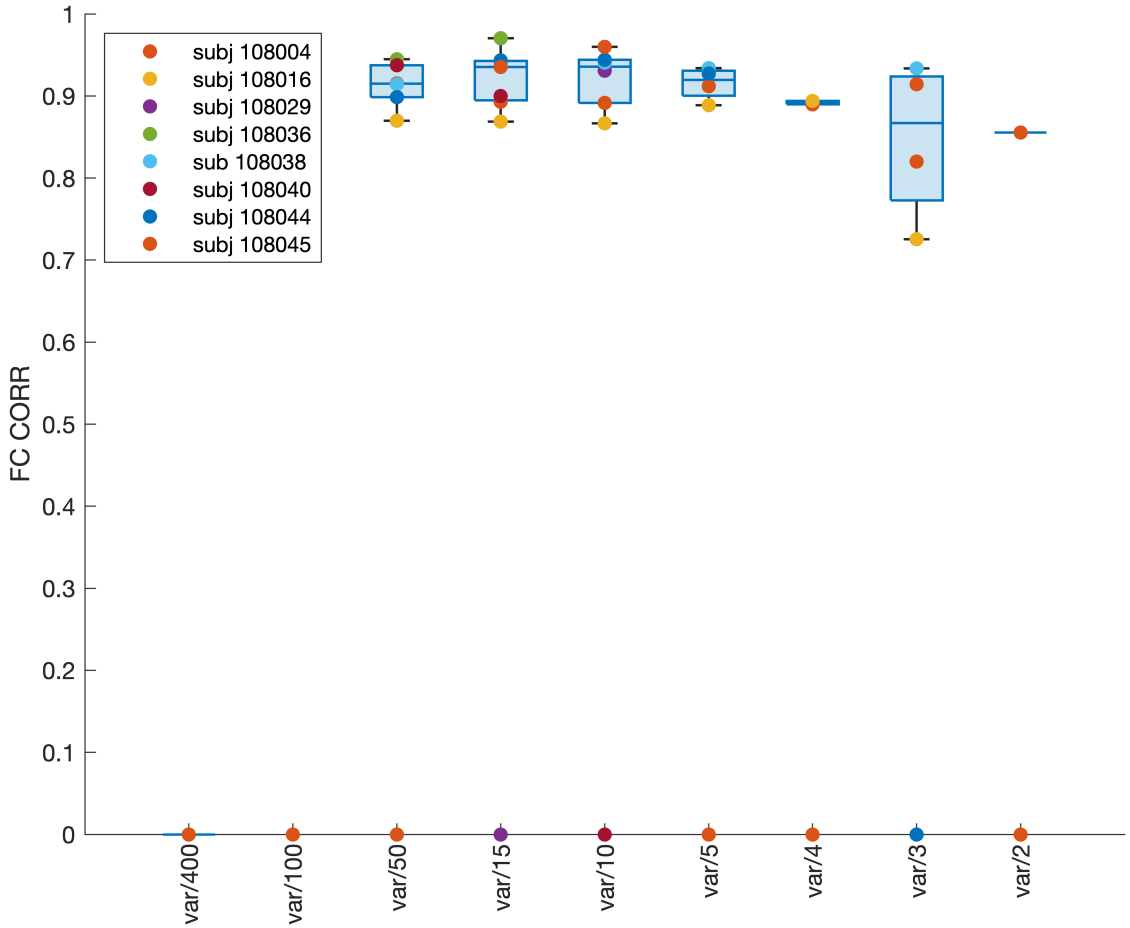

Figure 5.4: Empirical-estimated FC correlation through subjects. Visual representation of the FC correlation values through subjects for each weight of the noise variance . Mean values across subjects are represented in boxplot by horizontal lines.

After visually inspecting figures, namely (Fig.5.1)(Fig.5.2), values of *1/10, 1/15* were chosen. These values were selected based on criteria such as minimizing KS-distance and maximizing eFC-esFC correlation among subjects.
In addiction a value of *1/12* was took into consideration and used together with *1/10, 1/15* to estimate EC matrices in the whole dataset. During the estimation of effective connectivity (EC) matrices in the dataset, the algorithm faced convergence issues for some subjects. In instances where the algorithm converged with only one of the three weights of noise variance, the decision-making process was nuanced. Conversely, when convergence occurred for all three variance weight values, the selected value was the one that minimized KS-distance and maximized eFC-esFC correlation.

5.2 Correlation results

The purpose of the correlation analysis was to identify a significant relationship between effective connectivity derived metrics (Σ, Σ^{-1} and S) and metrics derived from [^{18}F]FDG PET (Metabolic Connectivity and SUVR).
Derived metrics were computed as described in 4.8.1 following the two approaches. First, the Spearman correlation between the strength values of Σ, Σ^{-1}, S, MC and SUVR were computed, considering each metric in both its original version (Fig.5.5) and in its absolute value (Fig. 5.6).

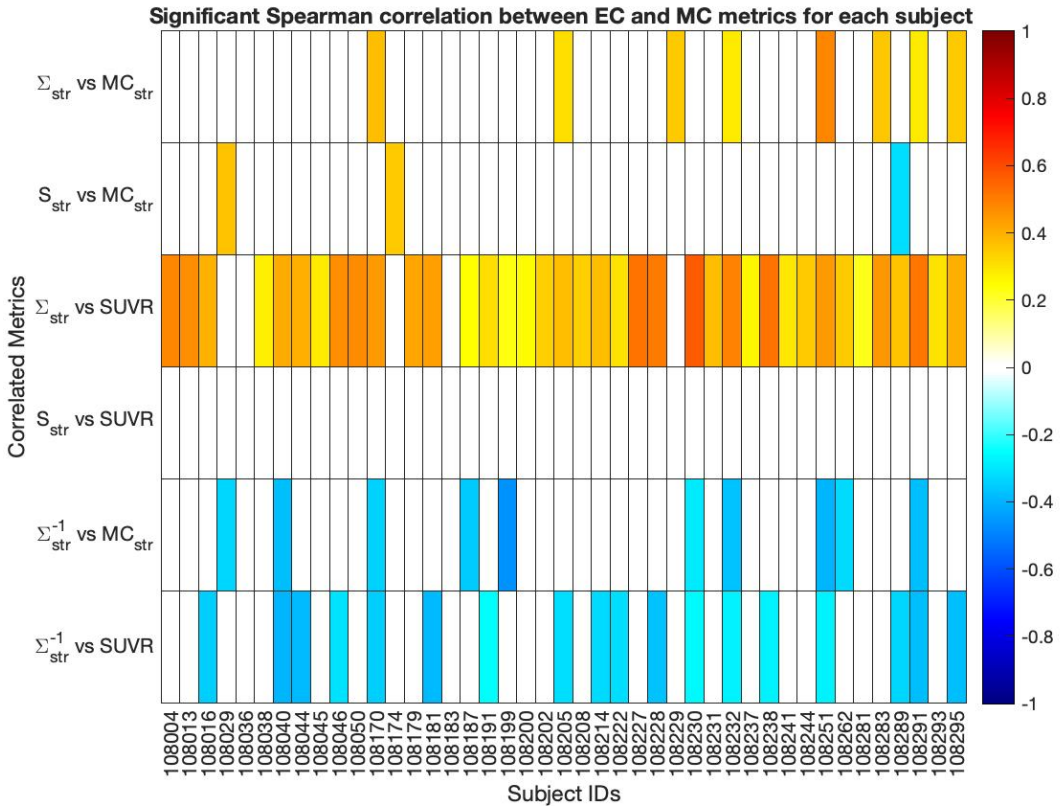

Figure 5.5: Spearman correlation between Σ_{str}, Σ^{-1}_{str}, S_{str}, MC_{str} and SUVR. Coupled-Spearman correlation was computed between Σ_{str}, Σ^{-1}_{str}, S_{str}, MC_{str} and SUVR. Correlation coefficients were corrected for multple comparison (FDR correction , alpha=0.05).
Positive values of correlation are represented in red while negative in blue.

Second, the Spearman correlation between upper triangular matrix of Σ, Σ^{-1}, S, MC and SUVR were computed , considering each metric both as its original formulation (Fig.5.7) and in its absolute value (Fig. 5.8). Correlations with SUVR were still computed considering the strength values of S, Σ^{-1} and Σ.

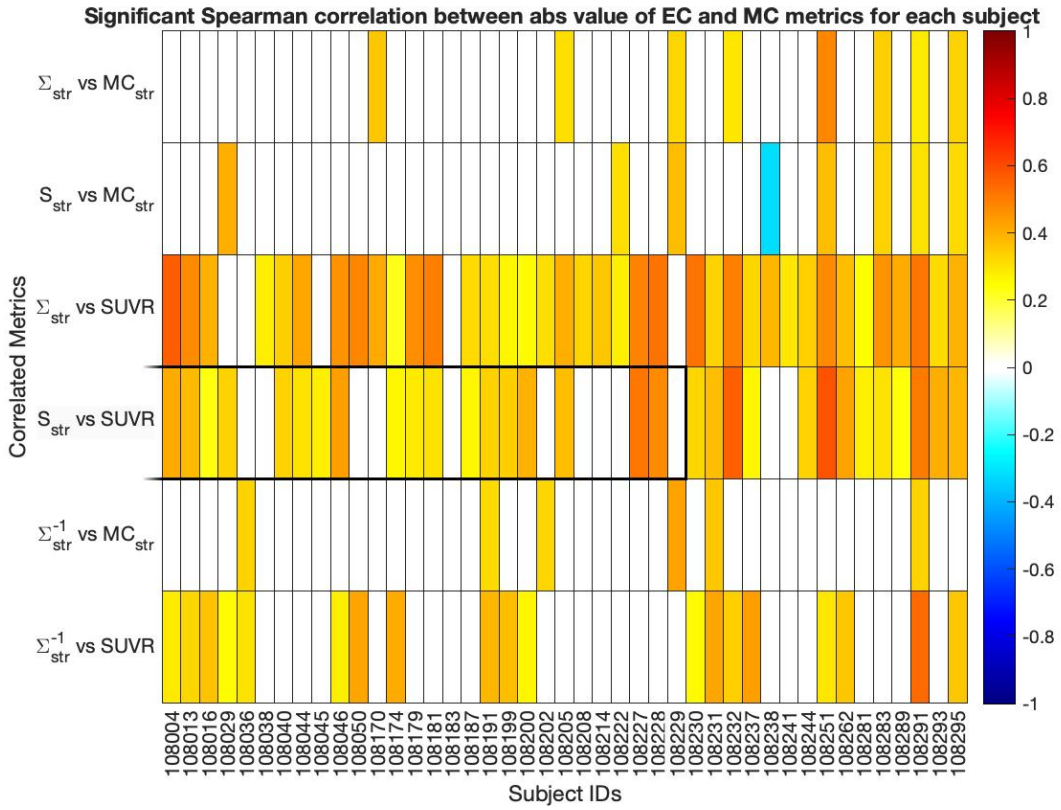

Figure 5.6: Spearman correlation between absolute values of Σ_{str}, Σ_{str}^{-1}, S_{str}, MC_{str} and SUVR. Coupled-Spearman correlation was computed between absolute values of Σ_{str}, Σ_{str}^{-1}, S_{str}, MC_{str} and SUVR. Correlation coefficients were corrected for multple comparison (FDR correction , alpha=0.05) Positive values of correlation are represented in red while negative in blue.

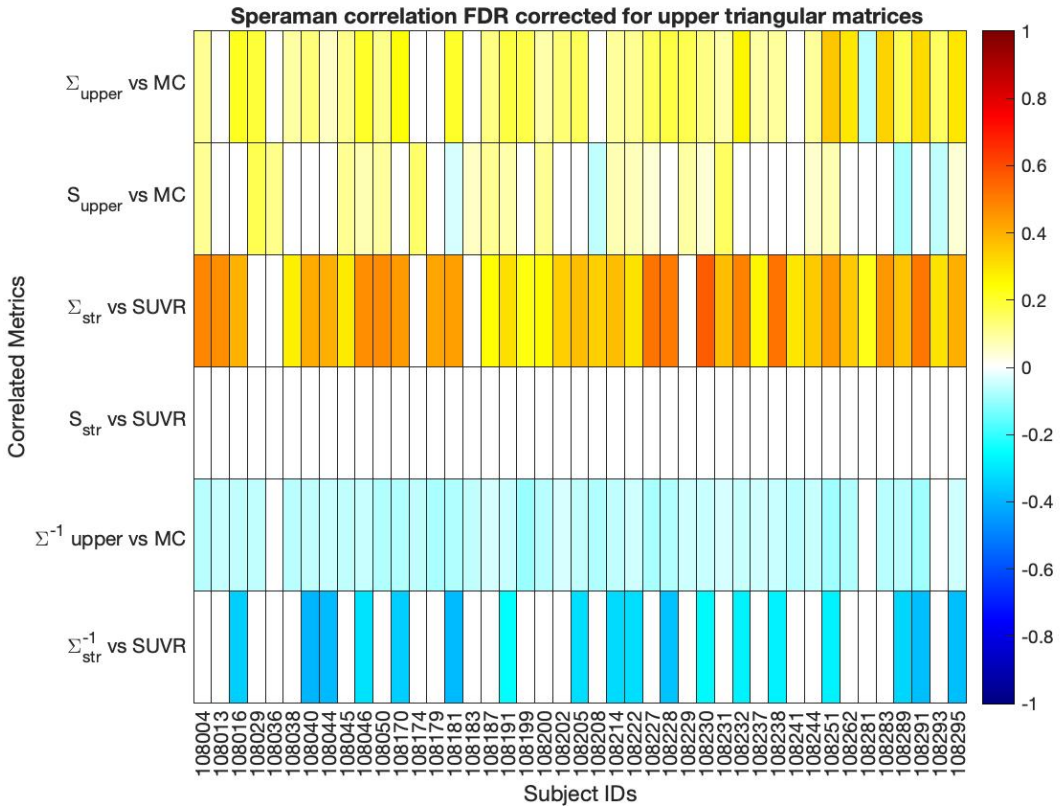

Figure 5.7: Spearman correlation between upper triangular matric of Σ, Σ^{-1}, S, MC and SUVR. Coupled-Spearman correlation was computed between upper triangular matrices of Σ^{-1}, S, MC . Correlation with SUVR metric was computed in terms of Σ_{str}, Σ^{-1}_{str}, S_{str}.Correlation coefficients were corrected for multiple comparison (FDR correction , alpha=0.05).
Positive values of correlation are represented from yellow to red while negative from light blue to blue.

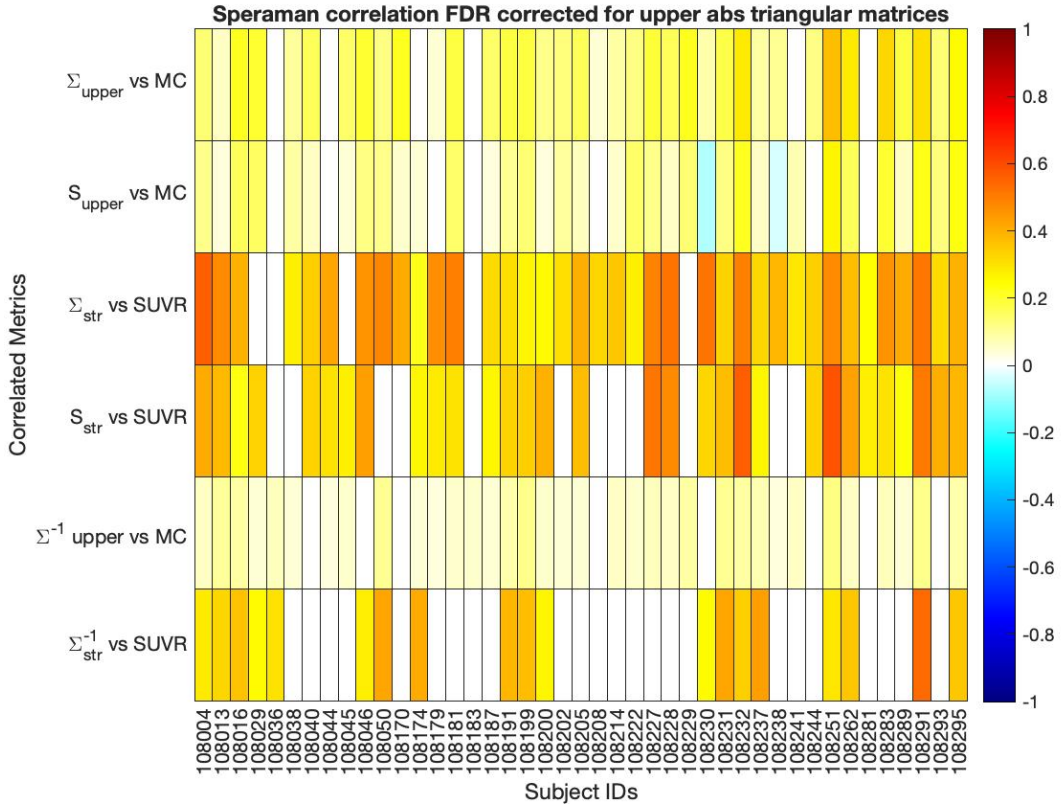

Figure 5.8: Spearman correlation between absolute values of upper triangular matric of Σ, Σ^{-1}, S, MC and SUVR. Coupled-Spearman correlation was computed between absolute values of upper triangular matrices of Σ^{-1}, S, MC . Correlation with SUVR metric was computed in terms of abslute values of Σ_{str}, Σ^{-1}_{str}, S_{str}.Correlation coefficients were corrected for multiple comparison (FDR correction , alpha=0.05).
Positive values of correlation are represented from green to red while negative in blue.

Subsequently, correlation analysis was carried out in and independent Oncology data set. Spearman correlation between the strength values of Σ, Σ^{-1}, S and SUVR, as well as between strength values of Σ, Σ^{-1}, S and MC were computed , considering each metric both as its original formulation (Fig.5.9) and in its absolute value (Fig. 5.10).

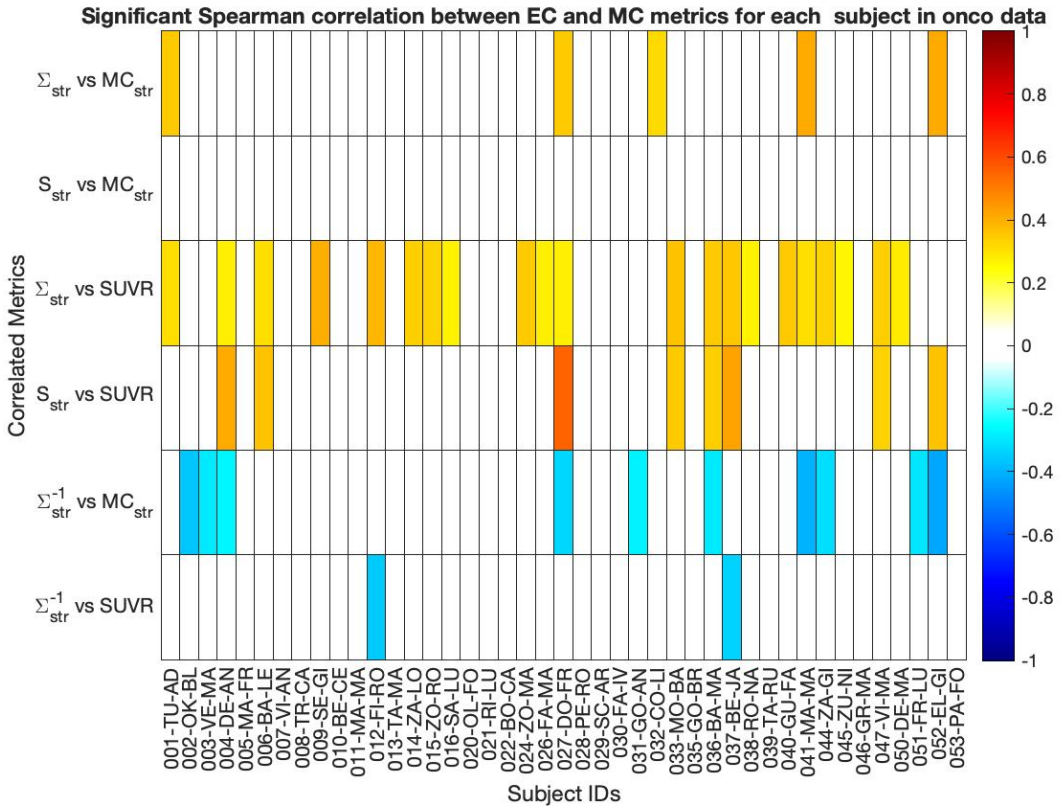

Figure 5.9: Spearman correlation between Σ_{str}, Σ^{-1}_{str}, S_{str}, MC_{str} and SUVR in an oncological dataset. Coupled-Spearman correlation was computed between Σ_{str}, Σ^{-1}_{str}, S_{str}, MC_{str} and SUVR. Correlation coefficients were corrected for multple comparison (FDR correction , alpha=0.05).
Positive values of correlation are represented in red while negative in blue.

Consistent monotonic relationship emerged considering both the strength values of Σ, Σ^{-1}, S, MC and SUVR (Fig.5.5), and their absolute value (Fig. 5.6). In particular positive-to-weak monotonic relationship between Σ_{str} and SUVR were observed, indicating a direct proportionality between the influence of a node within the entire brain network (in terms of Functional strenght) and the level of local glucose consumption at each node. Negative-to-weak monotonic relationship were found between Σ^{-1}_{str} and MC_{str} as well as for Σ^{-1}_{str} and SUVR.
No significant monotonic relationship were found between S_{str} and SUVR suggesting the independence between node predominant characteristic to act as source or sink and the level of local glucose consumption.(Fig. 5.6)
When considering the absolute values a weak to moderate monotonic positive rela-

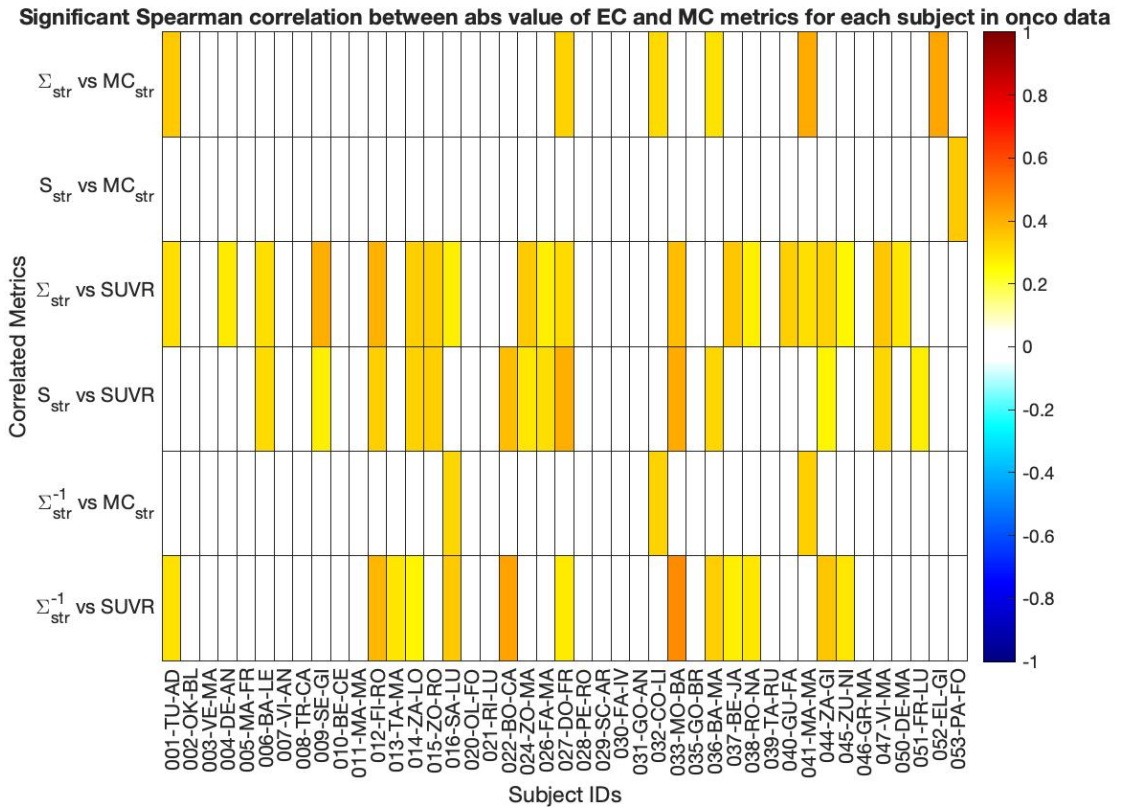

Figure 5.10: Spearman correlation between absolute values of Σ_{str}, Σ_{str}^{-1}, S_{str}, MC_{str} and SUVR in an oncological dataset. Coupled-Spearman correlation was computed between absolute values ofΣ_{str}, Σ_{str}^{-1}, S_{str}, MC_{str} and SUVR. Correlation coefficients were corrected for multple comparison (FDR correction , alpha=0.05).
Positive values of correlation are represented in red .

tionship emerged between S_{str} and SUVR, hence suggesting that local contribution of each node to global entropy production rate is proportionally related to the local level of glucose consumption. (Fig.5.7)
On the other hand weak positive and negative monotonic relationship emerged between respectively Σ_{upper} and MC, Σ_{upeer}^{-1} and MC suggesting a match behaviour between functional strength and the degree of coordination in metabolic activities between brain regions. Reduced relations between derived metrics were expected as effect of the tumor.(Fig. 5.9)5.10).
Accordingly, reduced moderate-to-weak monotonic positive relationship emerged when considering strength values of Σ and SUVR as well as reduced moderate-to-weak negative monotonic relationship between Σ_{str}^{-1} and MC_{str}. Spurious monotonic relationship appeared between Σ_{str} and MC_{str} as well as between Σ_{str}^{-1} and SUVR. No significant monotonic relationship has been found between S_{str} and MC_{str}.
Unexpectedly, a positive monotonic relationship manifested between S_{str} and SUVR. This suggests, in contrast to healthy patients, that the degree to which a node serves as a source or a sink is associated with local glucose consumption.
When considering the absolute values, a strengthening monotonic relationship

emerged between Σ_{str}^{-1} and SUVR as well as between S_{str} and SUVR. Conversely, a weakening monotonic relationship became apparent between Σ_{str}^{-1} and MC_{str}.

5.3 Wilcoxon results

Dissimilarity in median were tested for metrics computed in the correlation analysis of the HC and oncological dataset with a *Wilcoxon rank sum test*. The difference has been considered as significant if p-value$<$0.05.
A significant difference were found between: $\Sigma_{str} - SUVR$(p-value=0.0052)(Fig.5.11) and considering its absolute values (p-value=0.0181)(Fig5.12).

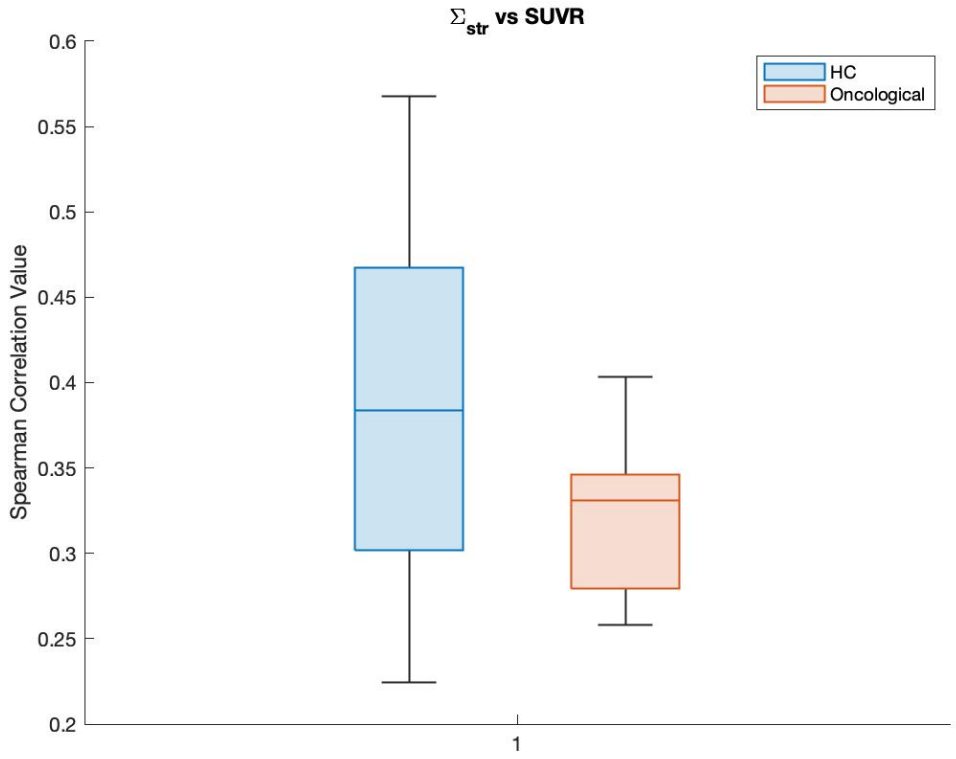

Figure 5.11: Wilcoxon ranksum test for correlation betweenΣ_{str}, Σ_{str}^{-1}, S_{str}, MC_{str} and SUVR. Significant difference in median were found between $\Sigma_{str} - SUVR$ HC and Oncological correlation values (p-value=0.0052)

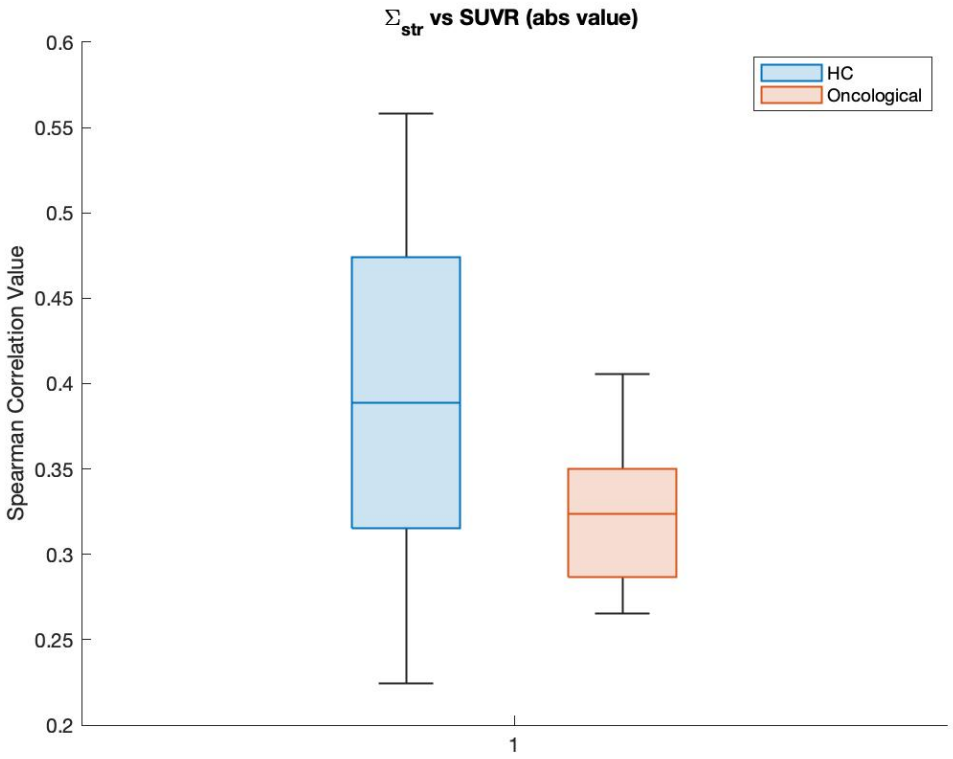

Figure 5.12: Wilcoxon ranksum test for cerrelation between absolute values of Σ_{str}, Σ_{str}^{-1}, S_{str}, MC_{str} and SUVR in HC and oncological subjects. Significant difference in median were found between absolute values of $\Sigma_{str} - SUVR$ HC and Oncological correlation values (p-value=0.0181)

Significant difference were found between upper triangular metrices of $S - MC$(p-value=0.0098), $\Sigma_{str}^{-1} - SUVR$(p-value=0.0052), $S_{str} - SUVR$(p-value=$2.2669 * e^{-12}$)and $\Sigma^{-1} - MC$(p-value=0.0046).(Fig.5.13)

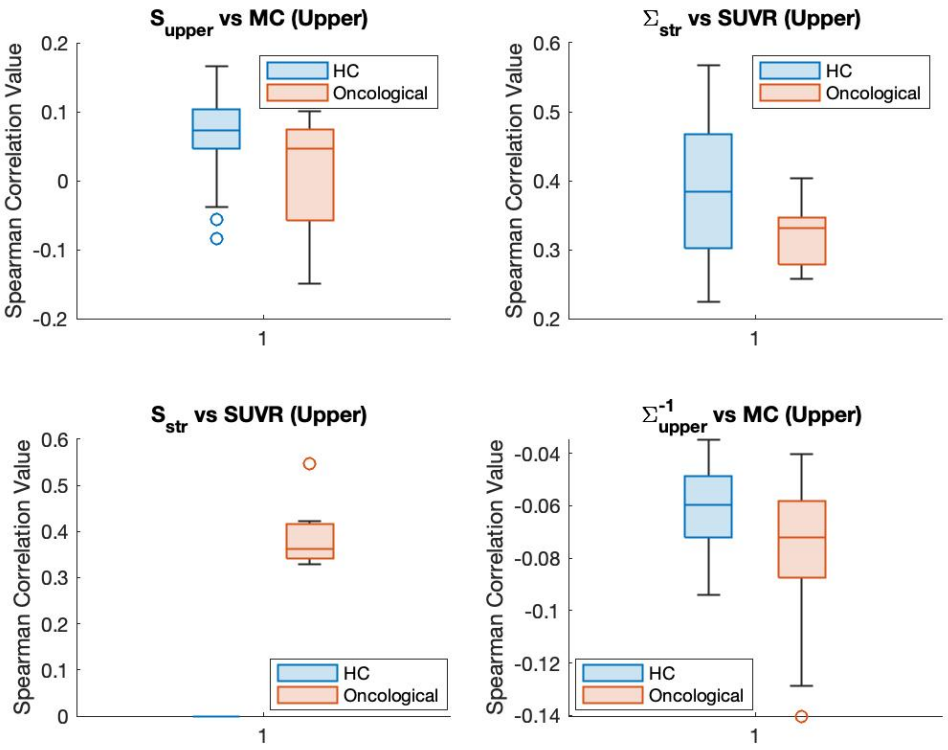

Figure 5.13: Wilcoxon ranksum test for correlation between upper triangular matrices of uΣ, Σ^{-1}, S, MC and SUVR in HC and oncological subjects. Correlation with SUVR metric was kept in terms of Σ_{str}, Σ_{str}^{-1}, S_{str}. Significant difference in median were found between correlation values of upper triangular matrices $S - MC$(p-value=0.0098), $\Sigma_{str}^{-1} - SUVR$(p-value=0.0052), $S_{str} - SUVR$(p-value=$2.2669 * e^{-12}$), $\Sigma^{-1} - MC$(p-value=0.0046) HC and oncological

Significant difference were found between absolute values of $\Sigma_{str} - SUVR$(p-value=0.0181) and upper triangular matrices $\Sigma^{-1} - MC$(p-value=0.0061).(Fig.5.14)

Overall the correlation values has been able to differentiate between oncology patients and healthy control , with the healthy patients characterized by higher correlations values than oncological subjects. Specifically, the strength of the monotonic relationship between a node's influence within the entire brain network, in terms of functional strength, and its local glucose consumption has remained consistently uniform across all correlated metrics. Therefore suggesting a higher decoupling between dissipative flow and local energy consumption in oncology patients.

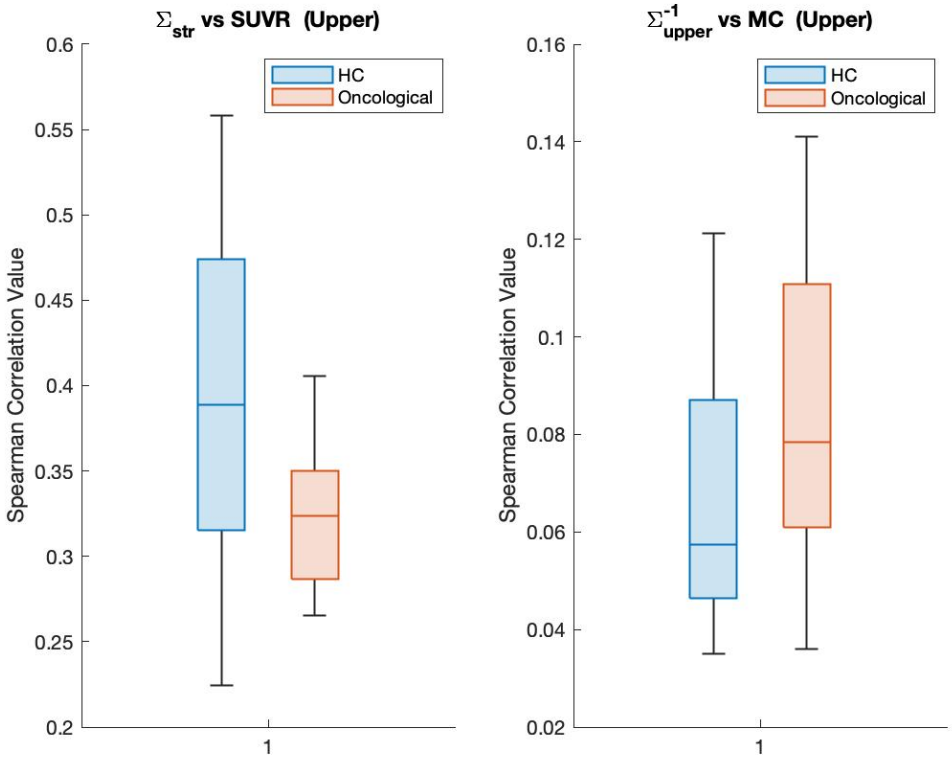

Figure 5.14: Wilcoxon ranksum test for correlation between absolute values of Σ, Σ^{-1}, S, MC and SUVR in HC and oncological subjects. Correlation with SUVR metric was kept in terms of Σ_{str}, Σ^{-1}_{str}, S_{str}. Significant difference in median were found between absolute values of upper triangular matrices $\Sigma_{str} - SUVR$(p-value=0.0181),$\Sigma^{-1} - MC$ HC and Oncological correlation values (p-value=0.0061)

5.4 Network contribution to effective-metabolic coupling

In this analysis, network-wise contribution to the correlation between $|S|_{str}$-SUVR (Fig. 5.15), Σ^{-1}_{str}-SUVR (Fig. 5.16), and between upper triangular matrices of $|S|$-MC (Fig. 5.22) and $\Sigma^{-1} - MC$ (Fig. 5.19) were isolated. This was done as these pairs of metric exhibited consistent conotonic relationship in the correlation analysis. Additionally, the point-to-line distances were computed between data points and regression line as metric of network influence on the correlation value. For semplicity, inter-network ROI were excluded from the point-to-line computation . The mean among point-to-line distances within the same network was chosen as subject-specific representative metric (Fig. 5.18)(Fig. 5.21).
For improved visualization, the aforementioned procedures were initially computed specifically for the data of **subject 108230**, given its consistent monotonic relationship across the considered correlations. On the other hand group-level network contribution to correlation are depicted in figures (Fig. 5.25)(Fig. 5.26)

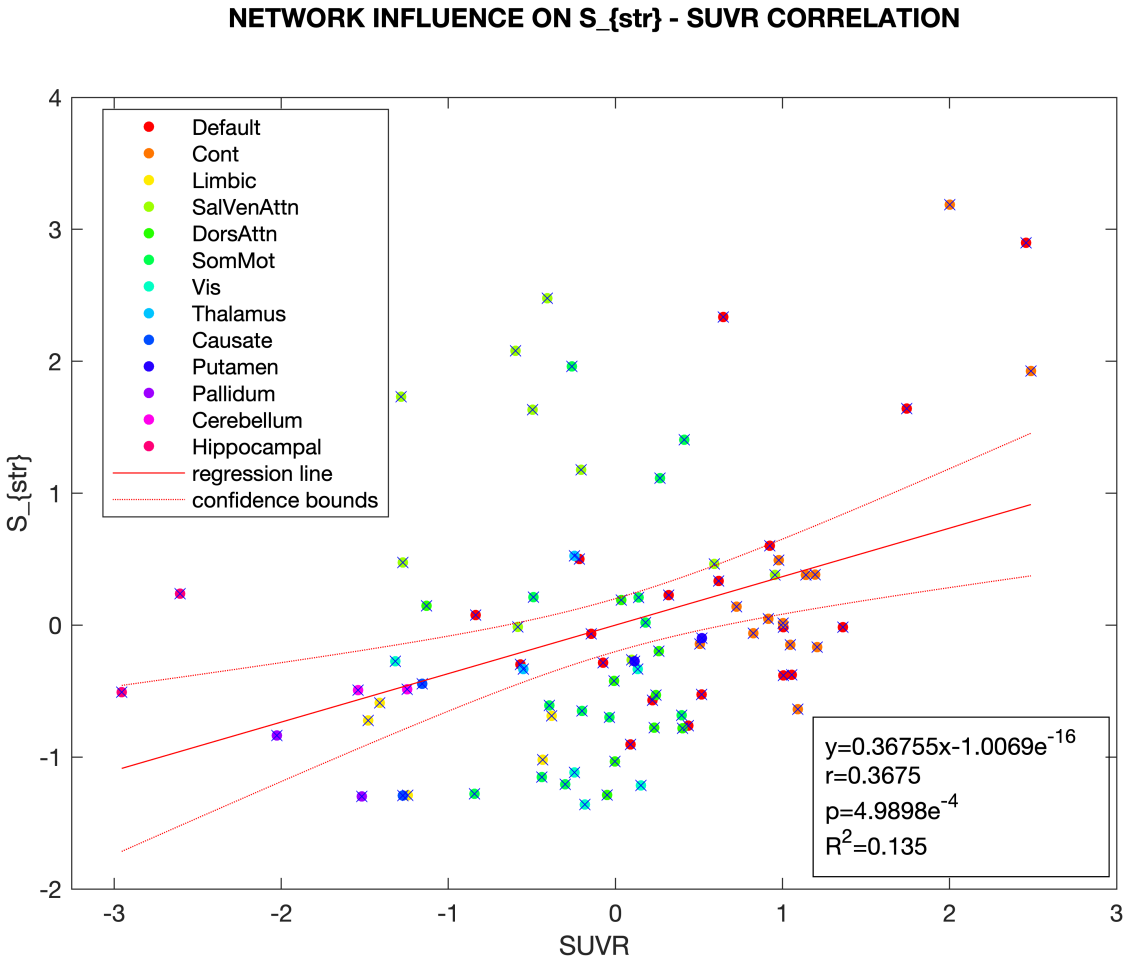

Figure 5.15: Networks influence on $S_{str} - SUVR$ correlation value. Visual representation of Network cluster around the regression line. Regression line is obtained fitting the data to a first-grade polynomial and quantify the relation between the two metrics

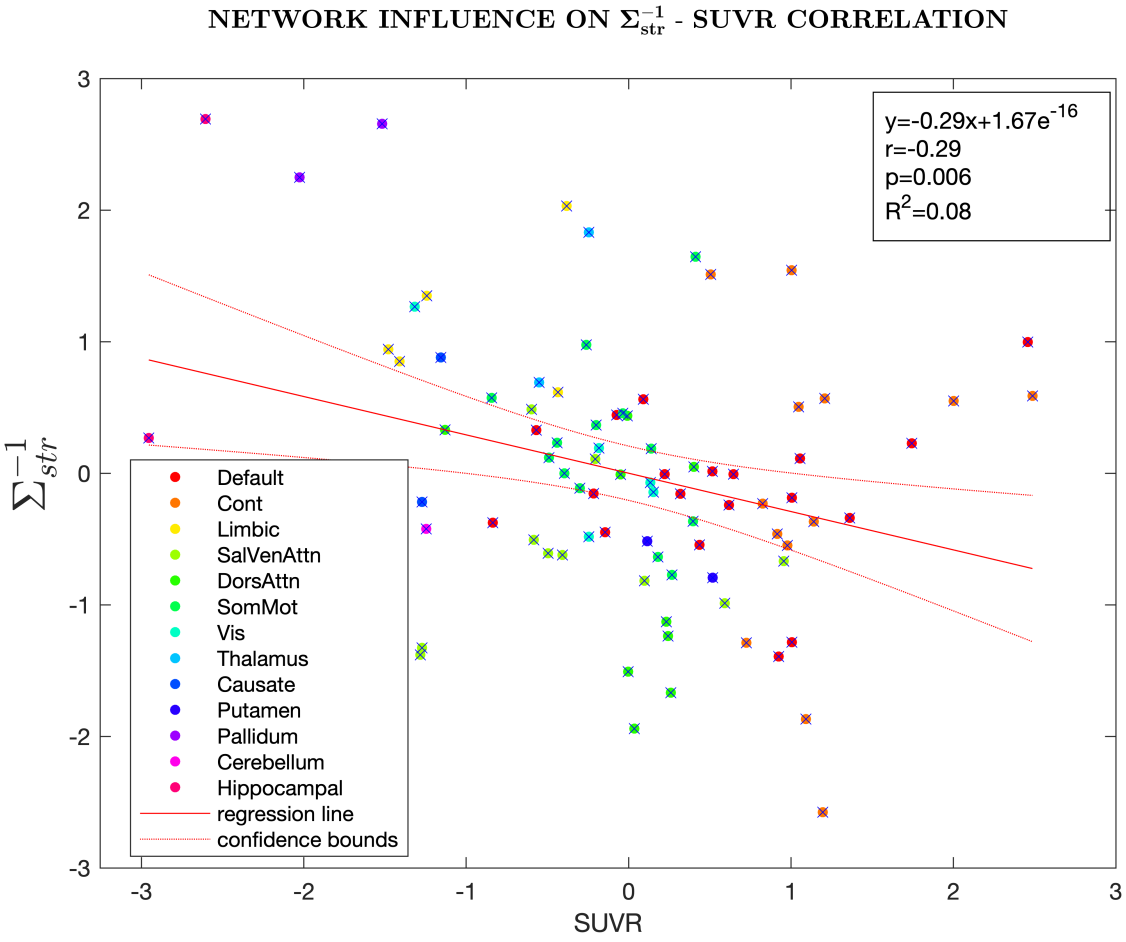

Figure 5.16: Networks influence on $\Sigma_{str}^{-1} - SUVR$ correlation value. Visual representation of Network cluster around the regression line. Regression line is obtained fitting the data to a first-grade polynomial and quantify the relation between the two metrics

All metrics have been zscored, by subtracting their mean and dividing for their standard deviation, for uniformity in measurement scale . After visual inspecting figure (Fig. 5.15) and figure (Fig. 5.16) linear relationship are assessed. Moderate significant linear relationship emerged (r=0.3675, $p_{value} = 4.9898e^{-4}$) when considering $|S|_{str}$ and SUVR, with the linearity driven by subcortical region of *Cerebellum, Hippocampal, Pallidum* and cortical regions of *Default, Cont, Vis and DorsAttn.* Overall cortical region has higher influences in the correlations between the two metric. However, only approximately 13.5% of the variability in the dependent variable is accounted for by the independent variable when considering a linear fit ($R^2 = 0.135$). Similar results were found in figure (Fig. 5.16) where a weak linear relationship emerged between Σ_{str}^{-1} and SUVR where subcortical regions of the *Pallidum, Cerebellum* as well as cortical regions of *Limbic, Vis, Cont, SalVenAttn* are influencing the correlation .
With respect to figure (Fig. 5.19) and figure (Fig. 5.22) significant weak linear relationship has been found between respectively Σ^{-1} and MC, and absolute values of MC and S. However, in both cases the independent variable could explain only

an extreme low proportion of the variance in the response variable. Overall it seems that cortical regions are the ones that influences the most the subject-specific correlation between the two metric .(See Fig.5.21 and Fig. 5.18)

Transitioning from subject-specific network contributions to correlation, our emphasis will now shift to group-level considerations. In contrast to earlier analyses, the linearity observed in the relationship between $|S|_{str}$ and $SUVR$ (Fig. 5.23) appears to be influenced by a broad contribution across networks, with a slight dominance in cortical regions of *SalVenAttn* and subcortical area of *Pallidum*, while the *Cerebellum* and *Hippocampal* regions exhibits the weakest contribution. In accordance with this, the linearity observed in the relationship between Σ^{-1}_{str} and $SUVR$ (Fig. 5.24) highlights a predominant contribution to de decoupling from the subcortical region of the *Cerebellum*, along with a minor contribution from the cortical region of the *Limbic* network. This suggests that the connection between the influence of a node within the brain network and local glucose uptake is primarily driven by subcortical regions, specifically the *Pallidum*.

On the other hand, a notable contribution from the *SalVenAttn* and *SomMot* networks emerged when exploring the relationship between the upper triangular matrix of Σ^{-1} and MC (Fig. 5.26). The cortical region of the *Pallidum* reaffirmed its significance in influencing this relationship.
Therefore, the subcortical area of the *Pallidum* prominently emerged as a key participant influencing the relationship in all linear correlations considered.

No group-level considerations were undertake regarding the relationship between the absolute values of S and MC as they didn't show a significant and consistent linear relationship among partecipant (30 subject with no significant Pearson correlation). This suggest the presence of a non-linear, monotonic relationship between the absolute values of S and MC.

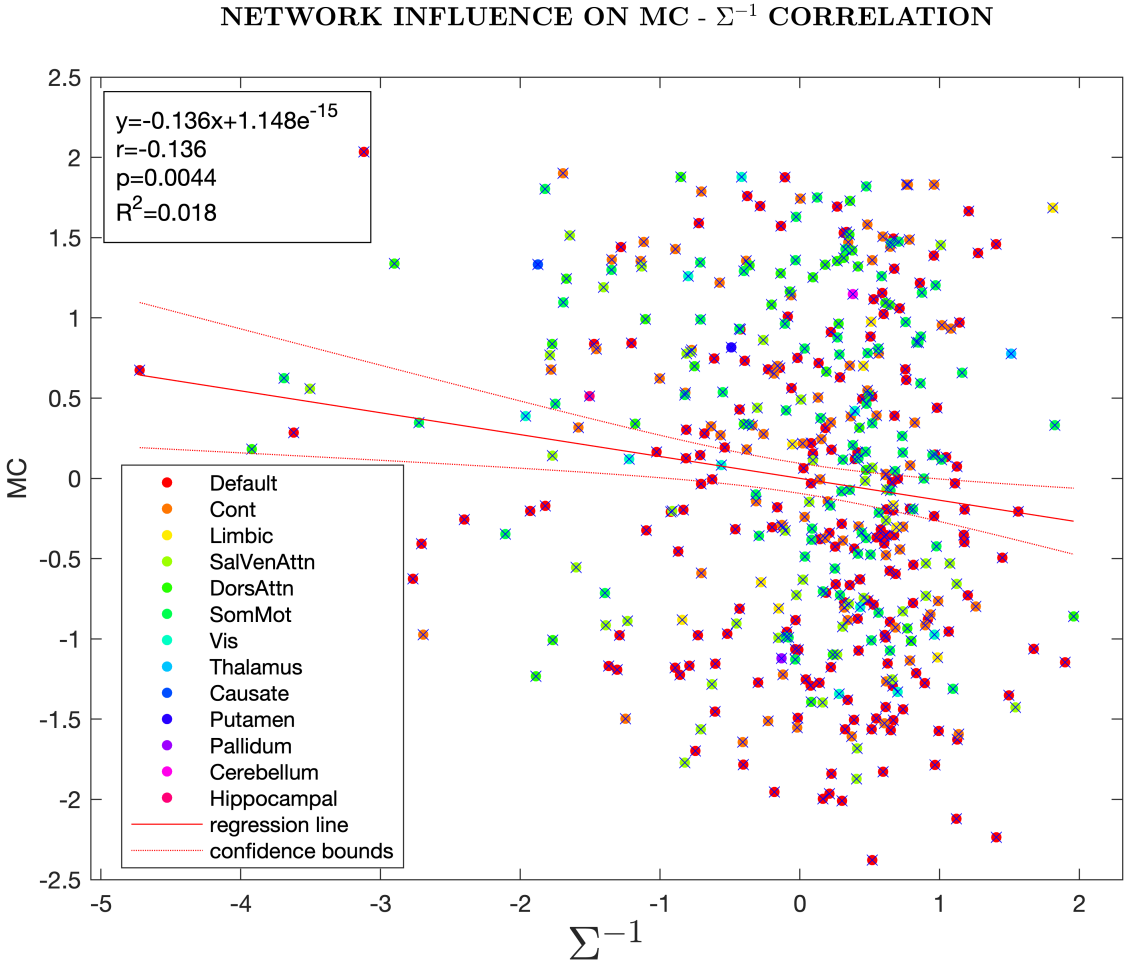

Figure 5.17: (a)

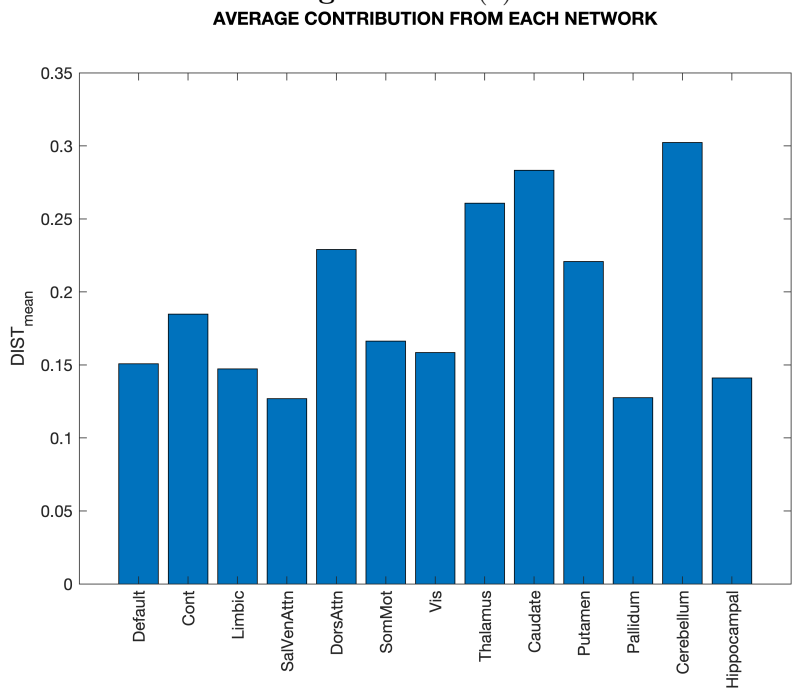

Figure 5.18: (b)

Figure 5.19: Intra-network measure of influence in the correlation between $\Sigma^{-1} - MC$. (a) Visual representation of intra-network contribution to the correlation. (b) Single subject Mean point-to-line distance from the regression line was computed among data within the same network (blue bar)

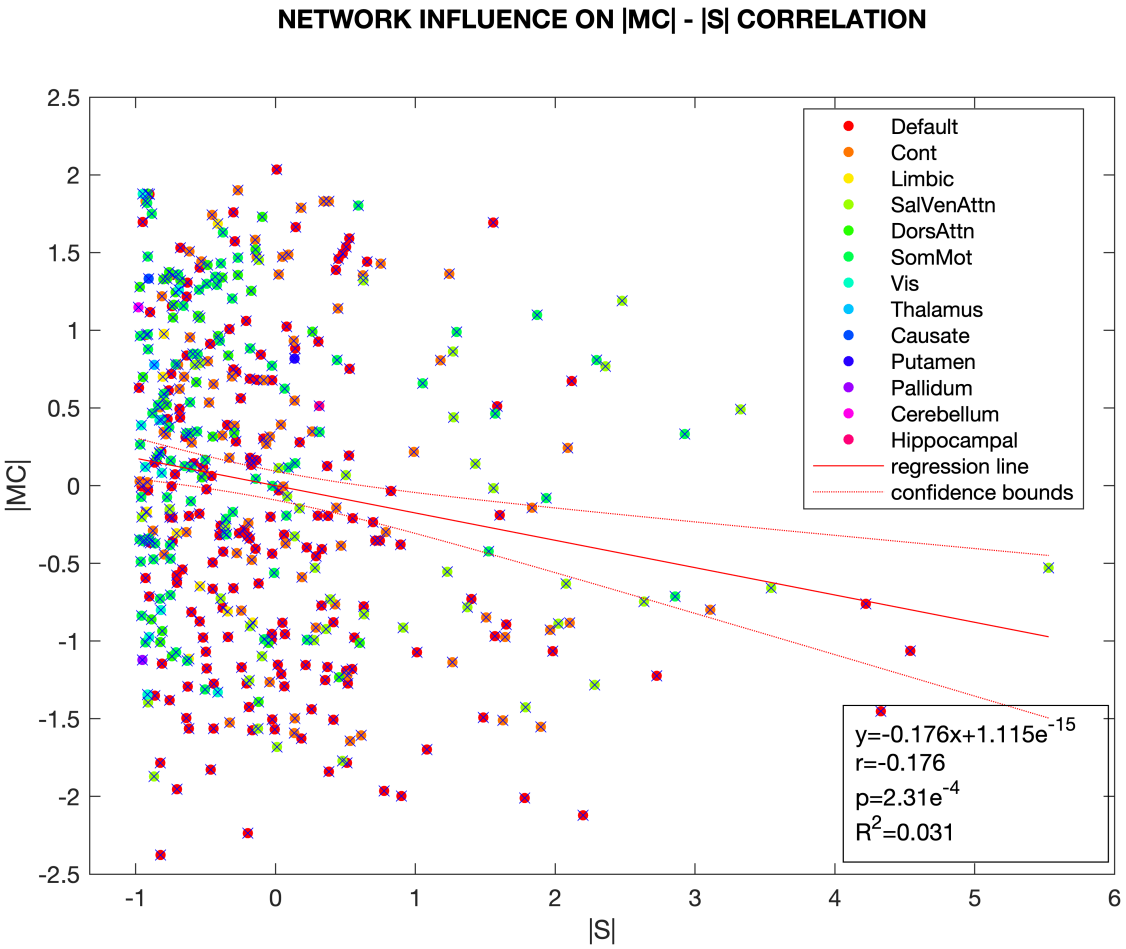

Figure 5.20: (a)

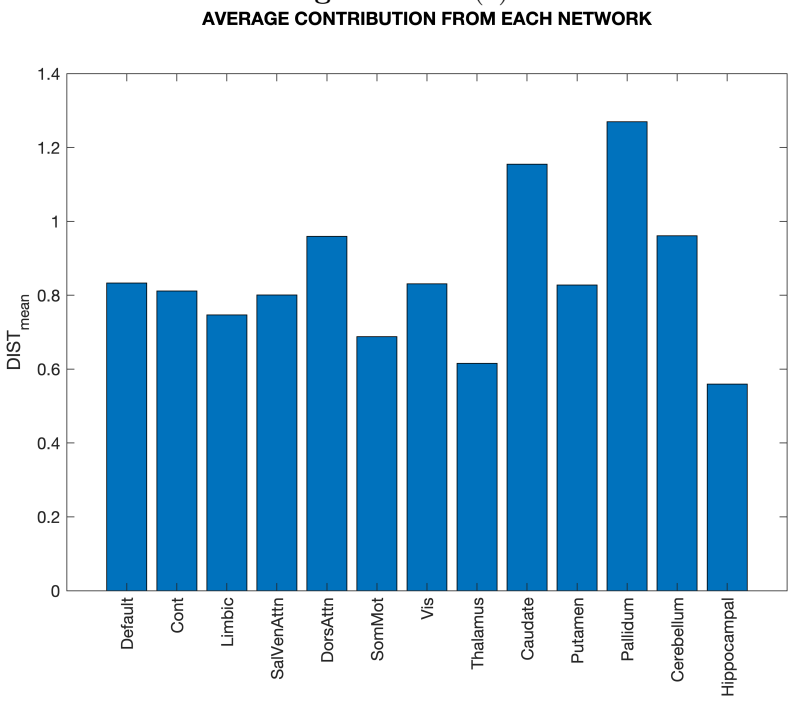

Figure 5.21: (b)

Figure 5.22: Intra-network measure of influence in the correlation between $|S| - |MC|$. (a) Visual representation of intra-network contribution to the correlation. (b) Single subject Mean point-to-line distance form the regression line was computed among data within the same network (blue bar)

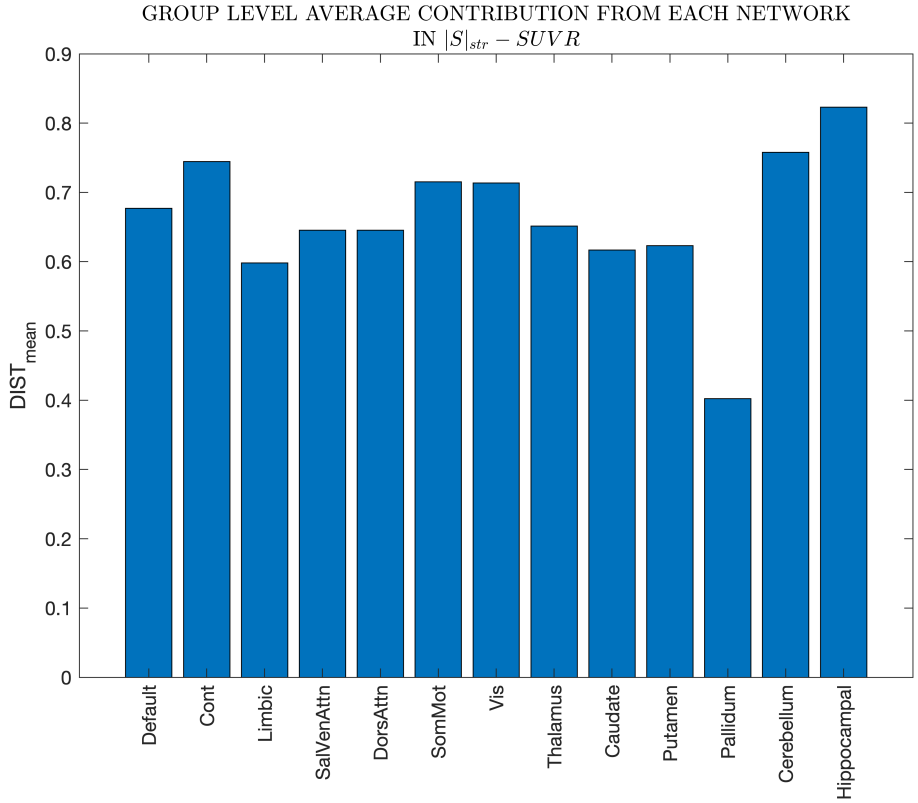

Figure 5.23: (a)

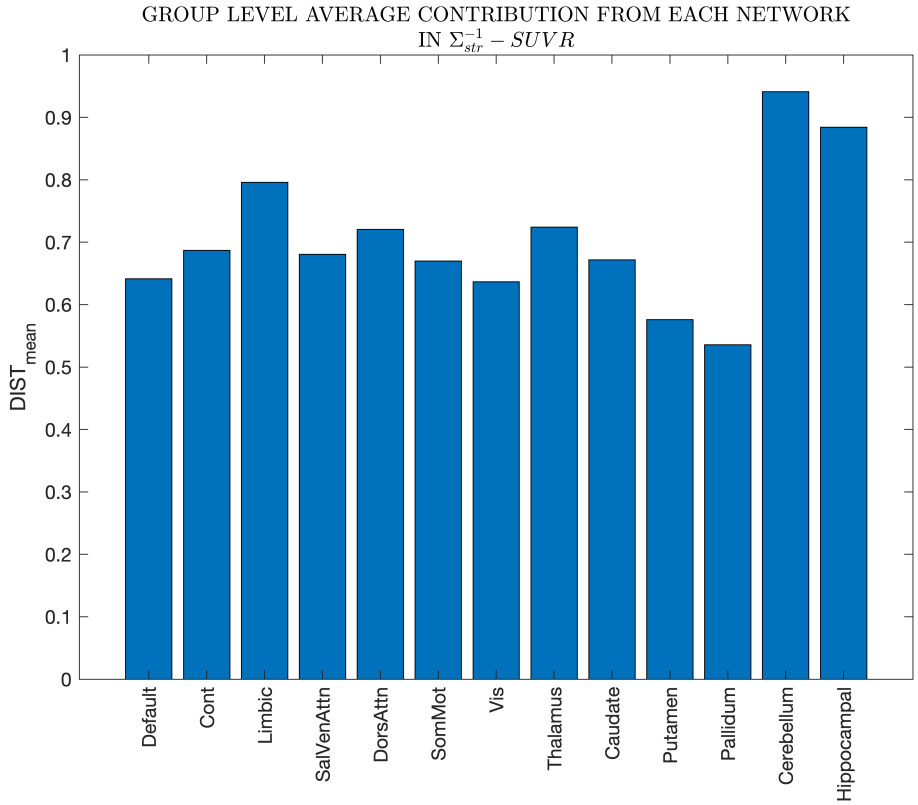

Figure 5.24: (b)

Figure 5.25: Group-level network contribution to correlation. Mean point-to-line distance form the regression line was computed among data within the same network (blue bar) and averaged among subjects. (a) group-level network contribution in $|S|_{str} - SUVR$ correlation (b) group-level network contribution in $\Sigma_{str}^{-1} - SUVR$ correlation

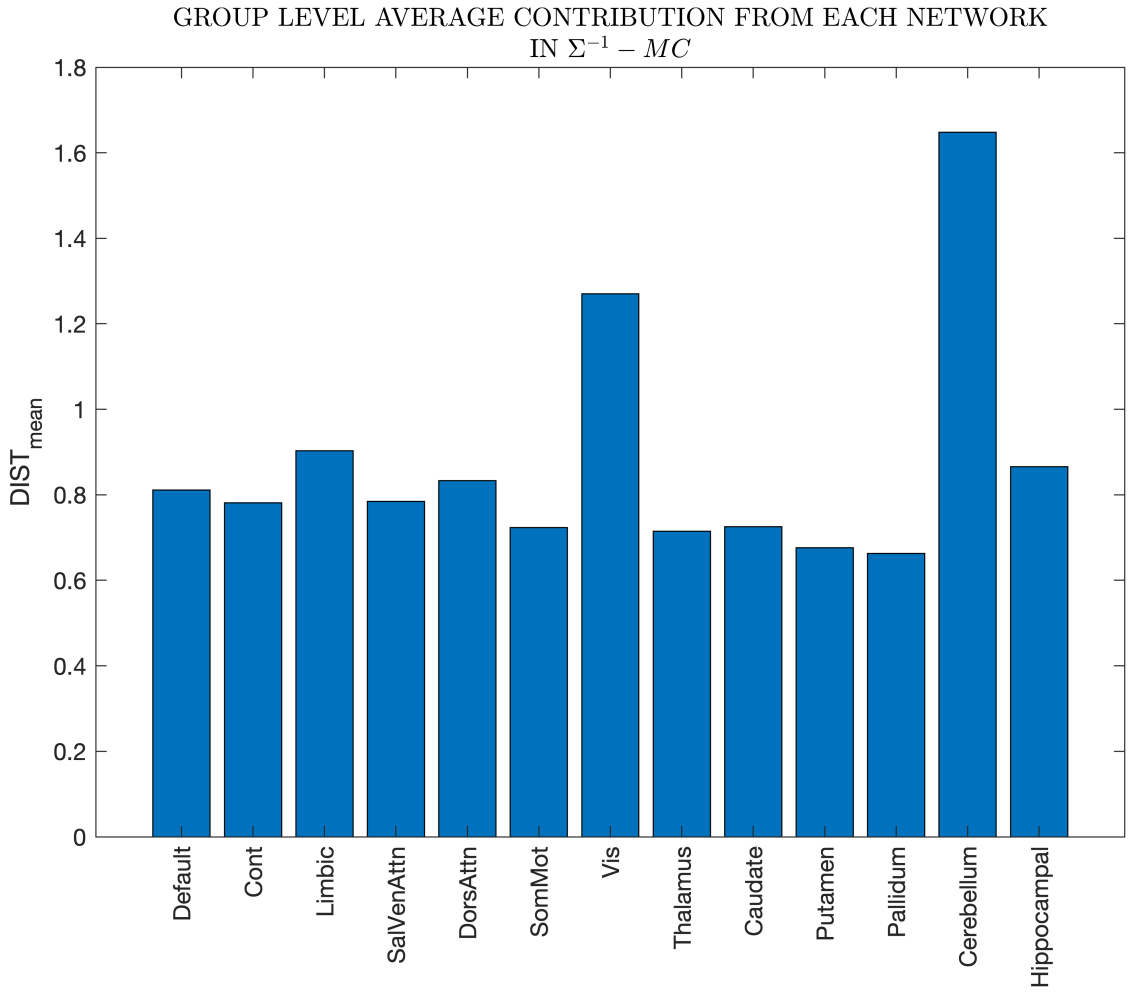

Figure 5.26: Group-level network contribution to correlation between upper triangular matrices Σ^{-1} and MC. Mean point-to-line distance form the regression line was computed among data within the same network (blue bar) and averaged among subjects.

Chapter 6

Discussion

In the upcoming section, we will engage in a detailed discussion of the results presented in the previous chapter. This discussion aims to provide insights into the estimated effective connectivity matrices and their decomposition into S, Σ and Σ^{-1}, along with their relationship between metabolic metrics (Metabolic Connectivity and SUVR). Additionally, we will offer insights into the comparison of discovered correlations between healthy and oncological subjects.

6.1 sparse DCM noise variance setup

As previously mentioned, the selection of the optimal noise variance in sparse DCM was based on finding a balance between empirical-estimated functional connectivity (eFC) correlation and empirical-estimated functional connectivity dynamics (FCD) Kolmogorov-Smirnov distance. This decision was informed by the results presented in figure (Fig. 5.1) and figure (Fig. 5.2), where eight reference subjects were considered. The subject-level analysis yielded a variable outcome, revealing that for both methods, the optimal weights of the noise variance that maximized the eFC-esFC factor and minimized the KS distance were either *1/10* or *1/15*.
This issue is likely primarily attributed to the higher sensitivity to noise in our original data, given the low TR (repetition time) and short timeseries. Consequently, this may lead to difficulties in accurately estimating the parameters of Dynamic Causal Modeling (DCM), affecting the reliability of the inferred connectivity patterns.

6.2 Correlation results

The purpose of this analysis was to evaluate possible relationships between effective connectivity derived metrics (Σ, Σ^{-1} and S) and metrics derived from [^{18}F]FDG PET (Metabolic Connectivity and SUVR).
There are few studies focusing on the decomposition of the effective connectivity matrix into Σ, Σ^{-1} and S matrices.
Consistent monotonic relationships across subjects emerged considering the strength values of Σ, Σ^{-1}, MC and SUVR. Specifically, positive-to-weak (r= 0.22-0.57) mono-

tonic relationship between Σ_{str} and SUVR were observed (Fig.5.5), indicating a direct proportionality between the influence of a node within the entire brain network (in terms of Functional strenght) and the level of local glucose consumption in each node.[37]
According to *Casti et al.,2023*[115] the Σ matrix represents the steady-state covariance matrix. In the context of connectivity, it characterizes the functional connectivity between brain regions by capturing statistical relationships and correlations among the neural activity signals of these regions without specifying the directionality of the connections.It has to be nothed that Under this interpretation, similar findings were reported in *Palombit et al.,2022* [12], where highly functionally connected regions (high FC strength) tended to exhibit higher SUVR values.
However, the the modest correlation between regional SUVR and strength of functional connections Σ_{str} between regions likely depends, also, on other factors including structural variables and local activity.[12]
As a matter of fact, FC is an indirect measure of structural connectivity [46][22], and its known to change with practice [31], possibly through activity-dependent plasticity [34]. Moreover, Recent studies found a moderate-strong relationship ($\rho \sim 0.4\check{}0.8$) between voxel-wise measures of local connectivity and/or activity based on fMRI signals (ALFF and ReHo) and SUVR at rest [75][76]. On the other hand, negative-to-weak monotonic relationship were found between Σ^{-1}_{str} and MC_{str} (r= -[0.46-0.29]) as well as for Σ^{-1}_{str} and SUVR (-[0.39-0.25]). (Fig.5.5) As stated by *Liégeois et al.,2020* [94] the Σ^{-1} matrix, also known as precision matrix, is able to quantify 'direct' statistical dependencies between variables and discard dependencies arising from intermediate connections captured in the correlation matrix Σ. Therefore, the negative-to-weak monotonic relationship mentioned above when interpreted Σ^{-1} in terms of partial correlation, becomes positive [94]. This suggests a directed proportionality between the influence of a node within the brain network on 'directed' statistical relationships and both local glucose level uptake and coordinated metabolic activity.
It has to be noted that the precision matrix has the important characteristic to be free from hemodynamic counfounding effects.
No significant monotonic relationship were found between S_{str} and SUVR suggesting either a non monotonic relationship or its absence between node predominant characteristic to act as source or sink and the level of local glucose consumption. However, when considered in its absolute value a positive-to-weak monotonic relationship emerged, hence suggesting that local contribution of each node to global temporal non-reversibility is proportionally related to the local level of glucose consumption.[37]

6.3 Wilcoxon results highlight differences between HC and Oncological subjects

Reduced relations between derived metrics were expected due to effect of the tumor.(Fig.5.9)(Fig.5.10) Previous studies have demonstrated that patients with brain tumors exhibit changes in functional connectivity (FC) as observed through resting-

state functional magnetic resonance imaging (rs-fMRI)[51][71]. These changes encompass distortion and alteration of resting-state networks due to tumor growth, a decrease in intra-hemispheric and inter-hemispheric FC within local networks, and alterations in cognitive function. Additionally, the presence of a tumor is associated with higher energy consumption levels[93]. Therefore, in addition to functional changes, it could lead to a decoupling between functional and metabolic activity.[51] Accordingly, reduced positive-to-weak monotonic relationship emerged when considering strength values of Σ and SUVR (r= 0.4-0.25) as well as reduced negative-to-weak monotonic relationship between Σ_{str}^{-1} and MC_{str} (r=-[0.42-0.27]).(Fig.5.9) This could probably be attributed to the tumor type and its location within the brain network.

Dissimilarity in median values was assessed by conducting a *Wilcoxon rank sum test* on the metrics computed in the correlation analysis of both the healthy control (HC) and oncological datasets. This statistical approach aimed to examine and compare the central tendencies of these metrics between the two datasets, shedding light on potential variations in their distributions and providing insights into the differences observed between the healthy and oncological subjects.

With a specific focus on the relationship between Σ and SUVR, it has consistently demonstrated the ability to differentiate between healthy and oncological patients, underscoring its potential as a diagnostic metric. Notably, a significant difference in median values (p-value = 0.0181) was identified, further supporting its discriminative capacity in distinguishing between the two groups.(Fig. 5.11)(Fig. 5.12)(Fig. 5.13)(Fig. 5.14)

Therefore, the variation in the strength of the monotonic relationship between the influence of nodes within the entire brain network (in terms of functional strength) and local glucose consumption implies a heightened decoupling between functional connectivity and correlated metabolic activity in oncological patients.

Accordingly, prior research has showcased the capability of functional connectivity (FC) in, classifying various pathologies [120], including different grade of gliomas [71], and in predicting survivability outcomes[122][50]. Additionally, SUV values has proven effective in differentiating among residual or higher grade brain tumor.[10] It also needs to be noted that considering the Σ matrix provides the advantage of having a functional connectivity cleaned from hemodynamic confounding effects that has been deconvoluted through DCM.

On the contrary, noteworthy positive distinctions in medians have surfaced when comparing the correlation of upper triangular matrices S with MC ($p_value = 0.0098$) and also between the upper triangular matrices of Σ^{-1} and MC. These observed differences in central tendencies underscore intriguing variations in the relationship patterns between healthy and oncological patient's metrics. The difference between upper triangular matrices S and MC could be interpreted as variations between solenoidal flow, differential covariance, and the synchronized metabolic activity correlations. As a matter of fact, metabolic connectivity has proven to be effective in differentiating among various dementia disorders through a differential analysis. This approach has demonstrated its utility in discerning distinctive patterns of metabolic activity that are associated with different types of dementia, providing valuable insights for accurate diagnosis and potential advancements in treatment strategies.[40][81]

6.4 Network contribution to effective-metabolic coupling

In this analysis, network-wise contribution to the correlation between $|S|_{str}$-SUVR (Fig. 5.15), Σ^{-1}_{str}-SUVR (Fig. 5.16), and between upper triangular matrices of $|S|$-MC (Fig. 5.22) and $\Sigma^{-1} - MC$ (Fig. 5.19) were isolated. Metrics related to oncological patients were excluded due to potential underlying modifications in the brain network, thereby resulting in inaccurate inference on network contribution to correlation.

Firstly, for simplicity, we focused on data specific to subject 108230, as it exhibits higher values among the measured correlations in the correlation analysis. Moderate significant linear relationship emerged (r=0.3675, $p_{value} = 4.9898e^{-4}$) when considering $|S|str$ and SUVR (Fig. 5.15), with the linearity driven by subcortical region of *Cerebellum, Hippocampal, Pallidum* and cortical regions of *Default, Cont, Vis and DorsAttn*. Overall cortical region have higher influences in the correlations between the two metric. However, only approximately 13.5% of the variability in the dependent variable is accounted for by the independent variable when considering a linear fit ($R^2 = 0.135$). With respect to figure (Fig. 5.19) and figure (Fig. 5.22) significant weak linear relationship has been found between respectively Σ^{-1} and MC, and absolute values of MC and S. However, in both cases the independent variable could explain only an extreme low proportion of the variance in the response variable. Overall it seems that cortical regions are the ones that influences the most the subject-specific correlation between the two metric .(See Fig.5.21 and Fig.5.18)

Considering the foregoing, we can deduce that the relationship between the metrics considered in the analysis is only partially linear. In-depth analyses are necessary to delve deeper into the topic. Moreover, checking for network contribution, each subject exhibited differences with spurious networks that kept a slight yet consistent influence on the correlation.

Secondly, our emphasis shifted to group-level considerations, seeking a broader understanding of the patterns and trends observed across the entire study cohort. This transition allowed for a comprehensive examination of collective behaviors, shedding light on shared characteristics and divergences that may arise when analyzing the data as a whole. The move from individual subjects to a group-level perspective adds a layer of complexity and richness to our exploration, providing a more holistic view of the interconnected relationships among the variables under scrutiny.

In contrast to earlier analyses, the linearity observed in the relationship between $|S|_{str}$ and $SUVR$ (Fig. 5.23) appears to be influenced by a broad contribution across networks, with a slight dominance in cortical regions of *Limbic* and subcortical area of *Pallidum*, while the *Cerebellum* and *Hippocampal* regions exhibits the weakest contribution. In accordance with this, the linearity observed in the relationship between Σ^{-1}_{str} and $SUVR$ (Fig. 5.24) highlights a predominant contribution from the subcortical region of the *Pallidum*, along with a minor contribution from the cortical region of the *SalVenAttn* network.

On the other hand, a notable contribution from the *Putamen* network emerged when exploring the relationship between the upper triangular matrix of Σ^{-1} and

MC (Fig. 5.26). The cortical region of the *Pallidum* reaffirmed its significance in influencing this relationship.
Overall, the subcortical area of the cerebellum prominently emerged as the weakest participant influencing the relationships in all linear correlations, diverging from its expected physiological importance.
In contrast to our finding, studies have demonstrated that the cerebellum plays a crucial role in cognitive functions such as attention, language, working memory, and executive functions.[28] It is involved in the prediction and coordination of movements, as well as the integration of sensory information. In particular, during resting state, the main role of the cerebellum is to participate in and synchronize various intrinsic connected networks involved in cognition and emotion, thus suggesting a consequent metabolic activation.[29] The neocerebellum, which includes lobules VII-VIII and the dentate nucleus, is functionally interconnected with non-motor associative cortices and serves as a major relay for these networks.Overall, the cerebellum is a complex structure that plays a vital role in both motor and non-motor functions.[27]
On the other hand, studies have affirmed our findings regarding the importance of the *Pallidum* region [8][108]. The ventral pallidum (VP) assumes a crucial role in regulating the default mode network (DMN) and controlling transitions between internally and externally guided behavior. Specifically, it is intricately involved in the switch between well-practiced, automatized behaviors that rely on internalized representations and behaviors that necessitate external focus. Functioning as a subcortical node of the DMN, the VP's modulation holds significant implications for attentional processes. Excitation of the VP has the potential to ensnare individuals in a DMN state of internally focused behavior, impairing their ability to direct attention to external stimuli. Conversely, inhibition of the VP facilitates task acquisition and allows for escape from the DMN brain state. This enables the seamless incorporation of external sensory information and enhances adaptability to the dynamic demands of the environment [8].
Therefore, the presence of the *Pallidum* across various correlations underscores its crucial contribution, highlighting the need for further investigation into the specific mechanisms and implications of its involvement in these linear relationships.
No group-level considerations were undertake regarding the relationship between the absolute values of S and MC as they didn't show a significant and consistent linear relationship among partecipant (30 subject with no significant Pearson correlation). This suggests the presence of either a non-linear, monotonic relationship or no relationship between the absolute values of S and MC.
It has to be noted that, based on our current knowledge, a comparison between the metrics we consider has never been attempted; therefore, any subsequent deduction is still in a preliminary phase.

Chapter 7

Conclusion

In this thesis, we characterized the relationships between the metrics derived from the decomposition of effective connectivity, metabolic connectivity, and SUVR. Our analysis revealed consistent correlations among the considered metrics and network influences in correlation, with a notable emphasis on the subcortical region of the *Pallidum* as a primary participant in these dynamics. Furthermore, through a comparative examination of healthy and oncological data, we demonstrated the potential for distinguishing between patient groups. In general, further investigations are necessary to optimize the analysis procedure and validate our preliminary findings. While the sparse DCM algorithm demonstrates its effectiveness at the individual level, the higher sensibility to noise of our data suggests the need for testing sparse DCM on a larger and diverse cohort. This step is crucial to ensure that our findings are not biased by the influence of a noisy component, thereby enhancing the generalizability and reliability of our results.
Additionally, a more in-depth characterization of the Σ matrix in terms of functional connectivity can be pursued by comparing connecting hubs and peripheral hubs. This nuanced exploration will provide valuable insights into the specific roles played by different brain regions in facilitating functional connections, contributing to a more comprehensive understanding of the interplay between effective connectivity and metabolic metrics identified in our study.
Furthermore, future studies can expand their scope to include a characterization of the relationship between effective connectivity metrics and SUVR with respect to tumor subpopulations. Investigating the influence of tumor type and location on these relationships can unveil potential variations in the neural network dynamics, contributing to a more tailored and nuanced interpretation of the findings. This approach allows for a more refined understanding of the intricate interplay between effective connectivity, metabolic activity, and the presence of tumors in the brain.
However, the existence of non-oxidative metabolic pathways underscores an imperfect coupling between oxygen and glucose utilization. This imperfection raises questions about the alignment between BOLD signals and glucose metabolism.[12] Furthermore, the debate over whether neurons or astrocytes serve as the principal executors in glucose metabolism remains an open issue. In light of these considerations, our studies, coupled with emerging discoveries in astrocyte specialized subpopulations whom are capable to function both as a neuron and glia [36], can provide a comprehensive physiological interpretation of the interplay between neural

networks and underlying metabolism in the brain
In conclusion, this exploration contributes to a deeper understanding of the intricate connections within the brain network, laying the groundwork for future research to explore the clinical implications and diagnostic potential of these identified relationships in diverse neurological conditions.

Acronyms

BOLD Blood Oxygen Level Dependent. 13

CMRGlu cerebral metabolic rate of glucose. 7

DCM Dynamic Causal Modelling. 11, 13, 17

EC Effective Connectivity. 12, 17, 18

EM Expectation maximization. 16, 18

HRF Hemodynamic Response Function. 17

IRCA interregional correlation analysis. 7

MIMO Multiple Input Multiple Output. 11

SUV standardized uptake value. 5

SUVR standardized uptake value ratio. 6

References

Books

[33] Arnold C.Paulino. *PET-CT in Radiotherapy Treatment Planning*. Saunders Elsiever, 2008 (cit. on p. 5).

[54] Luiping Wang Huges Garnier. *Identification of Continuos-time Models from Sampled Data*. Springer, 2008 (cit. on p. 18).

[87] P.Bennet, A.Mintz, B.Perry, A.Trout, and P.Vergara-Wentland. *Specialty Imaging: PET*. Elsevier, 2017 (cit. on p. 5).

[90] Giulia Pagnin. *Assessment of hemodynamic and connectivity alterations in brain gliomas through sparse DCM*. University of Padua, 2022 (cit. on pp. 27, 28).

Articles

[1] A.B.Patel, J.C.K.Lai, G.M.I.Chowdhury, F.Hyder, D.L.Rothman, R.G.Shulman, and K.L.Behar. "Direct evidence for activity-dependent glucose phosphorylation in neurons with implications for the astrocyte-to-neuron lactate shuttle". In: *Proc Natl Acad Sci U S A.* 111.14 (2014), pp. 5385–5390. DOI: 10.1073/pnas.1403576111 (cit. on p. 2).

[2] A.C.Marreiros, S.J.Kiebel, and K.J.Friston. "Dynamic causal modelling for fMRI: a two-state model. Neuroimage". In: *NeuroImage* 39.1 (2008), pp. 269–278. DOI: 10.1016/j.neuroimage.2007.08.019 (cit. on p. 17).

[3] A.Giorgio, L.Santelli, V.Tommassini, R.Bosnell, S.Smith, N.De Stefano, and H.Johansen-Berg. "Age-related changes in grey and white matter structure throughout adulthood". In: *NeuroImage* 51.3 (2010), pp. 943–951. DOI: 10.1016/j.neuroimage.2010.03.004.

[4] A.Gjedde and S.Marrett. "Glycolysis in neurons, not astrocytes, delays oxidative metabolism of human visual cortex during sustained checkerboard stimulation in vivo". In: *Journal of Cerebral Blood Flow and Metabolism* 21.12 (2001), pp. 1384–92. DOI: 10.1097/00004647-200112000-00002 (cit. on p. 2).

[5] A.Hahn et al. "Quantification of Task-Specific Glucose Metabolism with Constant Infusion of 18F-FDG". In: *Journal of Nuclear Medicine* 57.12 (2016), pp. 1933–1940. DOI: 10.2967/jnumed.116.176156.

[6] A.Hahn et al. "Reconfiguration of functional brain networks and metabolic cost converge during task performance". In: *eLife* 9.e52443 (2020). DOI: 10.7554/eLife.52443.

[7] A.Hahn et al. "Task-relevant brain networks identified with simultaneous PET/MR imaging of metabolism and connectivity". In: *Brain Struct Funct.* 223.3 (2018), pp. 1369–1378. DOI: 10.1007/s00429-017-1558-0 (cit. on p. 3).

[8] A.L.Klaassen, A.Heiniger, P.Vaca Sánchez, M.A.Harvey, and G.Rainer. "Ventral pallidum regulates the default mode network, controlling transitions between internally and externally guided behavior". In: *Proc Natl Acad Sci U S A* 118.36 (2021), e2103642118. DOI: 10.1073/pnas.2103642118 (cit. on p. 63).

[9] A.Nehlig, E.Wittendrop-Rechenmann, and C.D.Lam. "Selective Uptake of [14C]2-Deoxyglucose by Neurons and Astrocytes: High Resolution Microautoradiographic Imaging by Cellular 14C-Trajectography Combined With Immunohistochemistry". In: *Journal of Cerebral Blood Flow and Metabolism* 24.9 (2004), pp. 1004–1014. DOI: 10.1097/01.WCB.0000128533.84196.D8 (cit. on p. 2).

[10] A.Nozawa, A.H.Rivandi, M.Kanematsu, H.Hoshi, D.Piccioni, and S.Kesariand C.K.Hoh. "Glucose-corrected standardized uptake value in the differentiation of high-grade glioma versus post-treatment changese". In: *Nuclear Medicine Communications* 36.6 (2015), pp. 573–81. DOI: 10.1097/MNM.0000000000000288 (cit. on p. 61).

[11] D.B.Rubin A.P.Dempster N.M.Laird. "Maximum likelihood from incomplete data via the EM algorithm". In: *Royal Statistical Society Series B: Statistical Methodology* 39 (1977), p. 138. DOI: 10.1006/nimg.2001.1044 (cit. on p. 16).

[12] A.Palombit, E.Silvestri, T.Volpi, M.Aiello, D.Checchin, A.Bertoldo, and M.Corbetta. "Variability of regional glucose metabolism and the topology of functional networks in the human brain". In: *NeuroImage* 257 (2022), p. 119280. DOI: 10.1016/j.neuroimage.2022.119280 (cit. on pp. 60, 65).

[13] A.Savio et al. "Resting-State Networks as Simultaneously Measured with Functional MRI and PET". In: *Juournal of Nuclear Medicine* 58.8 (2017), p. 1314.1317. DOI: 10.2967/jnumed.116.185835 (cit. on p. 3).

[14] Buxton et al. "Dynamics of blood flow and oxygenation changes during brain activation: the balloon model". In: *Magn Reson Med* 39.6 (1998), pp. 855–64. DOI: 10.1002/mrm.1910390602 (cit. on p. 13).

[15] Friston et al. "Dynamic Causal Modelling". In: *NeuroImage* 19.4 (2003), pp. 1273–1302 (cit. on pp. 11–13, 16).

[16] Friston et al. "Nonlinear responses in fMRI: the Balloon model, Volterra kernels, and other hemodynamics". In: *NeuroImage* 12.4 (2000), pp. 466–77. DOI: 10.1006/nimg.2000.0630 (cit. on p. 13).

[17] R.L.Grubb et al. "The effects of changes in PaCO2 on cerebral blood volume, blood flow, and vascular mean transit time". In: *Stroke* 5.5 (1974), pp. 630–3. DOI: 10.1161/01.str.5.5.630 (cit. on p. 14).

[18] Stephan et al. "Dynamic causal models of neural system dynamics:current state and future extensions". In: *J Biosci.* 32.1 (2007), pp. 129–44. DOI: 10.1007/s12038-007-0012-5 (cit. on pp. 15–17).

[20] B.B.Biswal et al. "Toward discovery science of human brain function". In: *Proc Natl Acad Sci U S A* 107.10 (2010), pp. 4734–4739. DOI: 10.1073/pnas.0911855107.

[21] B.Horwitz, R.Duara, and S.I.Rapoport. "Intercorrelations of Glucose Metabolic Rates between Brain Regions: Application to Healthy Males in a State of Reduced Sensory Input." In: *Journal of Cerebral Blood Flow and Metabolism* 4.4 (1984), pp. 484–499. DOI: 10.1038/jcbfm.1984.73 (cit. on p. 7).

[22] B.Mišić, R.F.Betzel, A.Nematzadeh, J.Goni, A.Griffa, p:hagmann, A.Flammini, Y.Y.Ahn, and O.Sporns. "Cooperative and Competitive Spreading Dynamics on the Human Connectome". In: *Neuron* 86.6 (2015), pp. 1518–29. DOI: 10.1016/j.neuron.2015.05.035 (cit. on p. 60).

[23] B.T.Yeo et al. "The organization of the human cerebral cortex estimated by intrinsic functional connectivity." In: *Journal of Neurophysiology* 106.3 (2011). DOI: 10.1152/jn.00338.2011.

[24] C.Catana, A.R.Guimaraes, and B.R.Rosen. "PET and MR imaging: the odd couple or a match made in heaven?" In: *Journal of Nuclear Medicine* 54.5 (2013), pp. 815–824. DOI: 10.2967/jnumed.112.112771 (cit. on p. 3).

[25] C.Clark, R.carson, R.Kessler, R.Margolin, M.Buchsbaum, L.DeLisi, C.King, and R.Cohen. "Alternative statistical models for the examination of clinical positron emission tomography/fluorodeoxyglucose data". In: *Journal of Cerebral Blood Flow and Metabolism* 5.1 (1985), pp. 142–150. DOI: 10.1038/jcbfm.1985.18 (cit. on p. 7).

[27] C.Habas. "Functional Connectivity of the Cognitive Cerebellum". In: *Front Syst Neurosci* 15 (2021), p. 642225. DOI: 10.3389/fnsys.2021.642225 (cit. on p. 63).

[28] C.J.Stoodley, E.M.Valera, and J.D.Schmahmann. "Functional topography of the cerebellum for motor and cognitive tasks: an fMRI study." In: *NeuroImage* 59.2 (2012), pp. 1560–70. DOI: 10.1016/j.neuroimage.2011.08.065 (cit. on p. 63).

[29] C.J.Stoodley and J.D.Schmahmann. "Functional topography of the human cerebellum". In: *Handbook of Clinical Neurology* 154 (2018), pp. 59–70. DOI: 10.1016/B978-0-444-63956-1.00004-7 (cit. on p. 63).

[30] C.M.Clark and A.J.Stoessl. "Glucose use correlations: a matter of inference". In: *Juournal of Crebral Blood Flow and Metabolism* 6.4 (1986), pp. 511–512. DOI: 10.1038/jcbfm.1986.87 (cit. on p. 6).

[31] C.M.Lewis, A.Baldassarre, G.Committeri, G.L.Romani, and M.Corbetta. "Learning sculpts the spontaneous activity of the resting human brain". In: *Proc Natl Acad Sci U S A* 106.41 (2009), pp. 17558–63. DOI: 10.1073/pnas.0902455106 (cit. on p. 60).

[32] C.P.Chih and E.L.Roberts Jr. "Energy substrates for neurons during neural activity: a critical review of the astrocyte-neuron lactate shuttle hypothesis". In: *Journal of Cerbral Blood Flow and Metabolism* 23.11 (2003), pp. 1263–81. DOI: 10.1097/01.WCB.0000081369.51727.6F (cit. on p. 2).

[34] C.Sampaio-Baptista and H.Johansen-Berg. "White Matter Plasticity in the Adult Brain". In: *Neuron* 96.6 (2017), pp. 1239–1251. DOI: 10.1016/j.neuron.2017.11.026 (cit. on p. 60).

[35] C.Sprinz, S.Altmayer, M.Zanon, G.Watte, K.Irion, and E.Marchiori. "Effects of blood glucose level on 18F-FDG uptake for PET/CT in normal organs: A systematic review". In: *PLos ONE* 13.2 (2018). DOI: 10.1371/journal.pone.0193140.

[36] R.de Ceglia et al. "Specialized astrocytes mediate glutamatergic gliotransmission in the CNS". In: *Nature* 622 (2023), pp. 120–129. DOI: 10.1038/s41586-023-06502-w (cit. on p. 65).

[37] D.Benozzo, G.Baggio, G.Baron, A.Chiuso, S.Zampieri, and A.bertoldo. "Analyzing asymmetry in brain hierarchies with a linear state-space model of resting-state fMRI data". In: *bioRxiv* 565625 (2023). DOI: 10.1101/2023.11.04.565625 (cit. on pp. 31, 60).

[38] D.Peruzzo, A.Bertoldo, F.Zanderigo, and C.Cobelli. "Automatic selection of arterial input function on dynamic contrast-enhanced MR images". In: *Comput Methods Programs Biomed* 104.3 (2011), e148–57. DOI: 10.1016/j.cmpb.2011.02.0122 (cit. on p. 8).

[39] D.S.Lee, H.Kang, H.Kim, H.Park, J.S.Oh, J.S.Lee, and M.C.Lee. "Metabolic connectivity by interregional correlation analysis using statistical parametric mapping (SPM) and FDG brain PET; methodological development and patterns of metabolic connectivity in adults". In: *European Journal of Nuclear Medicine and Molecular Imaging* 35 (2008), pp. 1681–1691. DOI: 10.1007/s00259-008-0808-z (cit. on pp. 1, 7).

[40] D.Titov, J.Diehl-Schmid, K.Shi, R.Perneczky, N.Zou, T.Grimmer, J.Li, A.Drzezga, and I.Yakushev. "Metabolic connectivity for differential diag-

nosis of dementing disorders". In: *J Cereb Blood Flow Metab* 37.1 (2017), pp. 252–262. DOI: 10.1177/0271678X15622465 (cit. on p. 61).

[41] E.J.Metter, W.H.Riege, D.E.Kuhl, and M.E.Phelps. "Cerebral Metabolic Relationships for Selected Brain Regions in healthy Adults". In: *Journal of Cerebral Blood Flow and Metabolism* 1.4 (1984), pp. 1–7. DOI: 10.1038/jcbfm.1984.1 (cit. on p. 1).

[42] E.Silvestri, T.Volpi, A.Bettinelli, M.De Francisci, J.Jones, M.Corbetta, D.Cecchin, and A.Bertoldo. "Image-derived Input Function in brain [18F]FDG PET data: which alternatives to the carotid siphons?." In: *Annu Int Conf IEEE Eng Med Biol Soc.* (2022), pp. 243–46. DOI: 10.1109/EMBC48229.2022.9871200 (cit. on p. 8).

[43] G.A.Brooks, C.C.Carl, R.G.Leija, A.D.Osmond, J.J.Duong, and J.A.Arevalo. "Tracing the lactate shuttle to the mitochondrial reticulum". In: *Experimental and Molecular Medicine* 54 (2022), pp. 1332–1347. DOI: 10.1038/s12276-022-00802-3 (cit. on p. 2).

[44] G.Brix, J.Zaers, L.E.Adam, M.E.Bellemann, H.Ostertag, H.Trojan, U.Haberkorn, J.Doll andF.Oberdorfer, and W.J.Lorenz. "Performance evaluation of a whole-body PET scanner using the NEMA protocol". In: *Journal of Nuclear Medicine* 38.10 (1997), pp. 1614–23 (cit. on p. 26).

[45] G.Deco, A.Ponce-Alvarez, D.Mantini, G.L.Romani, P.Hagmann, and M.Corbetta. "Resting-State Functional Connectivity Emerges from Structurally and Dynamically Shaped Slow Linear Fluctuations". In: *Journal of Neurosciences* 33.27 (2013), pp. 11239–11252. DOI: 10.1523/JNEUROSCI.1091-13.2013.

[46] G.Deco, A.Ponce-Alvarez, D.Martini, G.L.Romani, P.Hagmann, and M.Corbetta. "Resting-state functional connectivity emerges from structurally and dynamically shaped slow linear fluctuations". In: *J Neurosci.* 33.27 (2013), pp. 11239–52. DOI: 10.1523/JNEUROSCI.1091-13.2013 (cit. on p. 60).

[47] G.Deco, M.L.Kringelbach, V.K.Jirsa, and P.Ritter. "The dynamics of resting fluctuations in the brain: metastability and its dynamical cortical core". In: *Scientific Reports* 7.3095 (2017). DOI: 10.1038/s41598-017-03073-5 (cit. on p. 30).

[48] G.Pagano, F.Niccolini, and M.Politis. "Current status of PET imaging in Huntington's disease". In: *Eur. J. Nucl. Med. Mol. Imaging* 46.6 (2016), pp. 1171–1182. DOI: 10.1007%2Fs00259-016-3324-6.

[49] G.Prando, M.Zorzi, A.Bertoldo, M. Corbetta, M. Zorzi, and A.Chiuso. "Sparse DCM for whole-brain effective connectivity from resting-state fMRI data". In: *NeuroImage* (2020), p. 208. DOI: 10.1016/j.neuroimage.2019.116367 (cit. on pp. 17, 18, 30, 31).

[50] G.Sprugnoli, L.Rigolo, M.Faria, P.Juvekar, Y.Tie, S.Rossi, N.Sverzellati, A.J.Golby, and E.Santarnecchi. "Tumor BOLD connectivity profile correlates

with glioma patients' survival". In: *Neurooncol Adv* 4.1 (2008), vdac153. DOI: 10.1093/noajnl/vdac153 (cit. on p. 61).

[51] H.A.Manan, E.A.Franz, and N.Yahya. "Functional connectivity changes in patients with brain tumours—A systematic review on resting state-fMRI". In: *Neurology, Psychiatry and Brain Research* 36 (2020), pp. 73–82. DOI: 10.1016/j.npbr.2020.03.003 (cit. on p. 61).

[52] H.F.Wehrl, M.Hossain, K.Lankes, C.C.Liu, I.Bezrukov, P.Martirosian, F.Schick, G.Reischl, and B.J.Pichler. "Simultaneous PET-MRI reveals brain function in activated and resting state on metabolic, hemodynamic and multiple temporal scales". In: *Nature Medicine* 19 (2013), pp. 1184–1189. DOI: 10.1038/nm.3290 (cit. on p. 3).

[53] H.F.Wehrl, S.Wiehr, M.R.Divine, S.Gatidis, G.T.Gullberg, F.C.Maier, A.M.Rolle, J.Schwenck, and W.M.Thaiss. "Preclinical and Translational PET/MR Imaging". In: *Journal of Nuclear Medicine* 55(Supplement 2) (2014), 11S–18S. DOI: 10.2967/jnumed.113.129221.

[55] I.Lundgaard et al. "Direct neuronal glucose uptake heralds activity-dependent increases in cerebral metabolism". In: *Nature Communications* 145 (2022), pp. 2276–2292. DOI: 10.1093/brain/awac174 (cit. on p. 2).

[56] I.Yakushev, A.Drzezga, and C.Habeck. "Metabolic connectivity: methods and applications". In: *Current Opinion in Neurology* 30.6 (2017), pp. 677–685. DOI: 10.1097/WCO.0000000000000494.

[57] J.Bock, A.Riedel, and K.Braun. "Differential changes of metabolic brain activity and interregional functional coupling in prefronto-limbic pathways during different stress conditions: functional imaging in freely behaving rodent pups". In: *Frontiers in Cellular Neuroscience* 6.19 (2012). DOI: 10.3389/fncel.2012.00019.

[58] J.Dauniezau, O.David, and K.E.Stephan. "Dynamic causal modelling: A critical review of the biophysical and statistical foundations". In: *NeuroImage* 58.2 (2011), pp. 312–322. DOI: 10.1016/j.neuroimage.2009.11.062 (cit. on p. 17).

[59] J.M.Ferreira, A.L.Burnett, and G.A.Rameau. "Activity-Dependent Regulation of Surface Glucose Transporter-3". In: *The Journal of Neuroscience* 31.6 (2011), pp. 1991–1999. DOI: 10.1523/JNEUROSCI.1850-09.2011.

[60] J.N.Keller, A.Germeyer, J.G.Begley, and M.P.Mattson. "17b-Estradiol Attenuates OxidativeImpairment of Synaptic Na1/K1-ATPaseActivity, Glucose Transport, and GlutamateTransport Induced by Amyloidb-Peptideand Iron". In: *Journal of Neuroscience Research* 50.4 (1997), pp. 522–530. DOI: 10.1002/(SICI)1097-4547(19971115)50:4<522::AID-JNR3>3.0.CO;2-G.

[61] J.R.Moeller, S.C.Strother, J.J.Sidtis, and D.A.Rottenberg. "Scaled subprofile model: a statistical approach to the analysis of functional patterns in

positron emission tomographic data". In: *Journal of Cerebral Blood Flow and Metabolism* 7.5 (1987), pp. 649–658. DOI: 10.1038/jcbfm.1987.118 (cit. on p. 7).

[62] J.S.Elam et al. "The Human Connectome Project: A retrospective". In: *NeuroImage* 244 (2021), p. 118543. DOI: 10.1016/j.neuroimage.2021.118543 (cit. on p. 26).

[63] J.Stender et al. "Quantitative rates of brain glucose metabolism distinguish minimally conscious from vegetative state patients". In: *Journal of Cerebral Blood Flow and Metabolism* 35.1 (2015), pp. 58–65. DOI: 10.1038/jcbfm.2014.169.

[64] K.Chen, D.Brandy, E.Reiman, S.C.Huang, M.Lawson, D.Feng, L.S.Yun, and A.Palant. "Noninvasive quantification of the cerebral metabolic rate for glucose using positron emission tomography, 18F-fluoro-2-deoxyglucose, the Patlak method, and an image-derived input function." In: *Journal of Cerebral Blood Flow and Metabolism* 18.7 (1998), pp. 716–23. DOI: 10.1097/00004647-199807000-00002 (cit. on p. 8).

[65] K.E.Stephan, L.Kasper, L.Harrison, J.Daunizeau, H.Den Ouden, M.Breakspear, and K.J.Friston. "Nonlinear dynamic causal models for fMRI". In: *NeuroImage* 42.2 (2008), pp. 649–662. DOI: 10.1016/j.neuroimage.2008.04.262 (cit. on p. 17).

[66] K.J.Friston. "Bayesian Estimation of Dynamical Systems: An Application to fMRI". In: *NeuroImage* 16 (2002), pp. 513–530. DOI: 10.1006/nimg.2001.1044 (cit. on p. 16).

[67] K.J.Friston, J.Kahan, B.Biswal, and A.Razi. "A DCM for resting state fMRI". In: *NeuroImage* 94 (2014), pp. 396–407. DOI: 10.1016/j.neuroimage.2013.12.009 (cit. on pp. 13, 17).

[68] K.Voigt, E.X.Liang, P.G.D.Ward, G.F.Egan, and S.D.Jamadar. "Metabolic and functional connectivity provide unique and complementary insights into cognition-connectome relationships". In: *Cerebral Cortex* 33 (2023), pp. 1476–1488. DOI: 10.1093/cercor/bhac150 (cit. on pp. 1, 2).

[69] L.Baowang and R.D.Freeman. "Neurometabolic coupling between neural activity, glucose, and lactate in activated visual cortex". In: *Journal of Neurochemistry* 6 (2015), p. 6807. DOI: 10.1038/ncomms78073.

[70] L.Hertz and Y.Chen. "Integration between Glycolysis and Glutamate-Glutamine Cycle Flux May Explain Preferential Glycolytic Increase during Brain Activation, Requiring Glutamate". In: *Frontiers of Integrative Neuroscience* 11.18 (2017), pp. 1–11. DOI: 10.3389/fnint.2017.00018.

[71] L.Pasquini, M.Jenabi, O.Yildirim, P.Silveira, K.K.Peck, and A.Holony. "Brain Functional Connectivity in Low- and High-Grade Gliomas: Differences in Network Dynamics Associated with Tumor Grade and Location". In: *Can-*

cers(Basel) 114.14 (2022), p. 3327. DOI: 10.3390/cancers14143327 (cit. on p. 61).

[72] L.Pellegrin and P.J.Magistretti. "Glutamate uptake into astrocytes stimulates aerobic glycolysis: A mechanism coupling neuronal activity to glucose utilization". In: *Proc. Natd. Acad. Sci. USA* 91.22 (1994), pp. 10625–10629. DOI: 10.1073%2Fpnas.91.22.10625.

[73] L.Rischka et al. "Reduced task durations in functional PET imaging with [18F]FDG approaching that of functional MRI". In: *NeuroImage* 181 (2018), pp. 323–330. DOI: 10.1016/j.neuroimage.2018.06.079.

[75] M.Aiello, E.Salvatore, A.Cachia, S.Pappatà, C.Cavaliere, A.Prinster, E.Nicolai, M.Salvatore, J.C. Baron, and M.Quarantelli. "Relationship between simultaneously acquired resting-state regional cerebral glucose metabolism and functional MRI: a PET/MR hybrid scanner study." In: *NeuroImage* 113 (2015), pp. 111–21. DOI: 10.1016/j.neuroimage.2015.03.017 (cit. on p. 60).

[76] M.Bernier, E.Croteau, C.A.Castellano, S.C.Cunnane, and K.Whittingstall. "Spatial distribution of resting-state BOLD regional homogeneity as a predictor of brain glucose uptake: A study in healthy aging". In: *NeuroImage* 150 (2017), pp. 14–22. DOI: 10.1016/j.neuroimage.2017.01.055 (cit. on p. 60).

[77] M.Castellaro, G.Rizzo, M.Tonietto, M.Veronese, F.E.Turkheimer, M.A.Chappell, and A.Bertoldo. "A Variational Bayesian inference method for parametric imaging of PET data". In: *NeuroImage* 150 (2017), pp. 136–149. DOI: 10.1016/j.neuroimage.2017.02.009.

[78] M.E.Raichle. "A brief history of human brain mapping". In: *Epub* 32.2 (2009), pp. 118–126. DOI: 10.1016/j.tins.2008.11.001.

[79] M.E.Raichle. "The restless brain". In: *Brain Connect* 1 (2011), pp. 3–12. DOI: 10.1089/brain.2011.0019. (cit. on p. 1).

[80] M.Jenkinson, P.Bannister, M.Brady, and S.Smith. "Improved optimization for the robust and accurate linear registration and motion correction of brain images". In: *NeuroImage* 7.2 (2002), pp. 825–41. DOI: 10.1016/s1053-8119(02)91132-8 (cit. on pp. 8, 27, 28).

[81] M.Scherr, L.Pasquini, G.Benson, R.Nuttall, M.Gruber, J.Neitzel, F.Brandl, and C.Sorg. "Decoupling of Local Metabolic Activity and Functional Connectivity Links to Amyloid in Alzheimer's Disease". In: *J Alzheimers Dis* 64.2 (2018), pp. 405–415. DOI: 10.3233/JAD-180022 (cit. on p. 61).

[82] M.Villien et al. "Dynamic functional imaging of brain glucose utilization using fPET-FDG". In: *NeuroImage* 100 (2014), pp. 192–199. DOI: 10.1016%2Fj.neuroimage.2014.06.025.

[83] Wiston M.Zhu, A.Neuhaus, D.J.Beard, B.A.Sutherland, and G.C.DeLuca. "Neurovascular coupling mechanisms in health and neurovascular uncoupling

in Alzheimer's disease". In: *Brain* 145 (2022), pp. 2276–2292. DOI: 10.1093/brain/awac174.

[84] N.Logothetis. "What we can do and what we cannot do with fMRI". In: *Nature* 453 (2008), pp. 869–878. DOI: 10.1038/nature06976.

[85] O.Sporns. "The human connectome: origins and challenges". In: *Neuroimage* 80 (2013), pp. 53–61. DOI: 10.1016/j.neuroimage.2013.03.023 (cit. on p. 2).

[86] O.Sporns, G.Tononi, and R.Kötter. "The human connectome: A structural description of the human brain". In: *PLoS Comput Biol.* 1.4 (2005), e42. DOI: 10.1371/journal.pcbi.0010042 (cit. on p. 2).

[88] P.D.Bridge and S.S.Sawilowsky. "Increasing Physicians' Awareness of the Impact of Statistics on Research Outcomes: Comparative Power of the t-test and Wilcoxon Rank-Sum Test in Small Samples Applied Research". In: *Journal of Clinical Epidemiology* 53.3 (1999). DOI: 10.1016/S0895-4356(98)00168-1 (cit. on p. 32).

[89] P.G.D.Ward, E.R.Orchard, S.Oldham, A.Arnatkevičiūtė, F.Sforazzini, A.Fornito, E.Storey, and G.F.Egan. "Individual differences in haemoglobin concentration influence bold fMRI functional connectivity and its correlation with cognition". In: *NeuroImage* 221 (2020), p. 117196. DOI: 10.1016/j.neuroimage.2020.117196 (cit. on p. 1).

[91] R.boellaard, N.C.Krak, O.S.Hoekstra, and A.A.Lammertsma. "Effects of noise, image resolution, and ROI definition on the accuracy of standard uptake values: a simulation study". In: *Journal of Nuclear Medicine* 45.9 (2004), pp. 1519–1527 (cit. on p. 6).

[92] R.H.R.Pruim, M.Mennes, D.van Rooij A.Llera, J.K.Buitelaar, and C.F.Beckmann. "ICA-AROMA: A robust ICA-based strategy for removing motion artifacts from fMRI data". In: *NeuroImage* 112 (2015), pp. 267–277. DOI: 10.1016/j.neuroimage.2015.02.064 (cit. on p. 26).

[93] R.J.Gilles, I.Robey, and R.A.Gatenby. "Causes and consequences of increased glucose metabolism of cancers". In: *Journal of nuclear medicine* 2 (2008), 24S–42S. DOI: 10.2967/jnumed.107.047258 (cit. on p. 61).

[94] R.Liégeois, A.Santos, V.Matta, D.Van De Ville, and A.H.Sayed. "Revisiting correlation-based functional connectivity and its relationship with structural connectivity". In: *Network Neuroscience* 4.4 (2020), pp. 1235–1251. DOI: 10.1162/netn_a_00166 (cit. on p. 60).

[95] R.Marchitelli et al. "Simultaneous resting-state FDG-PET/fMRI in Alzheimer Disease: Relationship between glucose metabolism and intrinsic activity". In: *NeuroImage* 176 (2018), pp. 246–258. DOI: 10.1016/j.neuroimage.2018.04.048.

[98] S.D.Jamadar, P.G.D.Ward, E.X.Liang, E.R.Orchard, Z.Chen, and G.F.Egan. "Metabolic and hemodynamic resting-state connectivity of the human brain:

a high-temporal resolution simultaneous BOLD-fMRI and FDG-fPET multimodality study". In: *Cerebral Cortex* 31.6 (2021), pp. 2855–2867. DOI: 10.1093/cercor/bhaa393.

[99] S.D.Jamadar, P.G.D.Ward, G.CThomas, F.Alex, M.Premaratne, K.O'Brien, D.Stäb, Z.Chen, N.J.Shah, and G.F.Egan. "Monash rsPET-MRI". In: *OpenNeuro* (2020b). DOI: https://doi.org/10.18112/openneuro.ds002898.v1.1.1.

[100] S.D.Jamadar, P.G.D.Ward, S.Li, F.Sforazzini, J.Baran, Z.Chen, and G.F.Egan. "Simultaneous task-based BOLD-fMRI and [18-F] FDG functional PET for measurement of neuronal metabolism in the human visual cortex". In: *NeuroImage* 189 (2019), pp. 258–266. DOI: 10.1016/j.neuroimage.2019.01.003 (cit. on p. 3).

[101] S.D.Jamadar, P.G.D.Ward, T.G.Close, A.Fornito, M.Premaratne, K.O'Brien, D.Stäb, Z.Chen, N.J.Shah, and G.F.Egan. "Simultaneous BOLD-fMRI and constant infusion FDG-PET data of the resting human brain." In: *Scientific Data* 7.1 (2020), p. 363. DOI: 10.1038/s41597-020-00699-5.

[102] S.G.Kim and S.Ogawa. "Biophysical and physiological origins of blood oxygenation level-dependent fMRI signals". In: *J Cereb Blood Flow Metab* 32.7 (2012), pp. 1188–206. DOI: 10.1038/jcbfm.2012.23.

[103] S.Genc, I.A.Kurnaz, and M.Ozilgen. "Astrocyte - neuron lactate shuttle may boost more ATP supply to the neuron under hypoxic conditions - in silico study supported by in vitro expression data". In: *BMC Syst Biol* 5 (2011). DOI: 10.1186/1752-0509-5-162.

[104] S.J.Kiebel, M.Garrido, and K.J.Friston. "Dynamic causal modelling of evoked responses: the role of intrinsic connections". In: *NeuroImage* 36.2 (2007b), pp. 332–345. DOI: 10.1016/j.neuroimage.2007.02.046 (cit. on p. 17).

[105] S.J.Kiebel, S.Kloppel, N.Weiskopf, and K.J.Friston. "Dynamic causal modelling: a generative model of slice timing in fMRI". In: *NeuroImage* 34.4 (2007a), pp. 1487–1496. DOI: 10.1016/j.neuroimage.2006.10.026 (cit. on p. 17).

[106] S.M.Smith et al. "Correspondence of the brain's functional architecture during activation and rest". In: *PNAS* 106.31 (2009), pp. 13040–13045. DOI: 10.1073/pnas.0905267106.

[107] S.N.Vaishnavi, A.G.Vlassenko, M.M.Rundle, A.Z.Snyder, M.A.Mintun, and M.E.Raichle. "Regional aerobic glycolysis in the human brain". In: *Proc Natl Acad Sci U S A* 107.41 (2010), pp. 17757–62. DOI: 10.1073/pnas.1010459107 (cit. on p. 26).

[108] S.Robinson, G.Basso, N.Soldati, U.Sailer, J.Jovicich, L.Bruzzone, I.Kryspin-Exner, H.Bauer, and E.Moser. "A resting state network in the motor control circuit of the basal ganglia". In: *BMC Neuroscience* 10 (2009), p. 137. DOI: 10.1186/1471-2202-10-137 (cit. on p. 63).

[109] S.Ryali, T.Chen, A.Padmanabhan, W.Cai, and V.Menon. "Development and validation of consensus clustering-based framework for brain segmentation using resting fMRI". In: *Journal of Neuroscience Methods* 240 (2015), pp. 128–40. DOI: 10.1016/j.jneumeth.2014.11.014 (cit. on pp. 23, 24).

[110] T.J.Turek, R.A.Hawkins, and J.E.Wilson. "Correlation of hexokinase content and basal energy metabolism in discrete regions of rat brain". In: *Journal of Neurochemistry* 46.3 (1997), pp. 983–985. DOI: 10.1111/j.1471-4159.1986.tb13066.x.

[111] T.T.Liu. "Noise contributions to the fMRI signal: An overview". In: *NeuroImage* 143 (2016), pp. 141–151. DOI: 10.1016/j.neuroimage.2016.09.008.

[112] T.Volpi, E.Silvestri, M.Corbetta, and A.Bertoldo. "Assessing different approaches to estimate single-subject metabolic connectivity from dynamic [18F]fluorodeoxyglucose Positron Emission Tomography data". In: *Annu Int Conf IEEE Eng Med Biol Soc.* (2021), pp. 3259–3262. DOI: 10.1109/EMBC46164.2021.9630441 (cit. on pp. 7, 8).

[113] T.Volpi, G.Vallini, E.Silvestri, M.Francisci, T.Durbin, M.Corbetta, J.J.Lee, A.G.Vlassenko, M.S.Goyal, and A.Bertoldo. "A new framework for metabolic connectivity mapping using bolus [18F]FDG PET and kinetic modeling". In: *Journal of Cerebral Blood Flow and Metabolism* 271678X231184365 (2023). DOI: 10.1177/0271678X231184365 (cit. on pp. 8, 9, 26).

[114] T.Watanabe and J.Hatazawa. "Evaluation of Functional Connectivity in the Brain Using Positron Emission Tomography: A Mini-Review". In: *Frontiers in Neuroscience* 13.775 (2019). DOI: 10.3389/fnins.2019.00775.

[115] U.Casti, G.Baggio, D.Benozzo, S.Zampieri, A.Bertoldo, and A.chiuso. "Dynamic Brain Networks with Prescribed Functional Connectivity". In: *arXiv* 2310.07262 (2023) (cit. on pp. 31, 60).

[116] V.D.Calhoun and J.Sui. "Multimodal fusion of brain imaging data: A key to finding the missing link(s) in complex mental illness". In: *Biol Psychiatry Cogn Neurosci Neuroimaging* 1.3 (2016), pp. 230–244. DOI: 10.1016/j.bpsc.2015.12.005 (cit. on p. 3).

[117] V.Riedl, L.Utz, G.Castillón, T.Grimmer, J.P.Reuschecker, M.Ploner, K.J.Friston, A.Drzezga, and C.Sorg. "Metabolic connectivity mapping reveals effective connectivity in the resting human brain". In: *PNAS* 113.2 (2016), pp. 428–433. DOI: 10.1073/pnas.1513752113 (cit. on p. 2).

[118] W.Meng, J.R.Tobin, and D.W.Busija. "Glutamate-Induced Cerebral Vasodilation Is Mediated by Nitric Oxide Through N-Methyl-d-Aspartate Receptors". In: *Stroke* 26.5 (1995), pp. 857–863. DOI: 10.1161/01.STR.26.5.857.

[119] X.Yan et al. "Homotopic local-global parcellation of the human cerebral cortex from resting-state functional connectivity". In: *NeuroImage* 273 (2023), p. 120010. DOI: 10.1016/j.neuroimage.2023.120010 (cit. on pp. 23, 25).

[120] Y.Du, Z.Fu, and V.D.Calhoun. "Classification and Prediction of Brain Disorders Using Functional Connectivity: Promising but Challenging". In: *Front Syst Neurosci* 12 (2018). DOI: 10.3389/fnins.2018.00525 (cit. on p. 61).

[121] Y.Sagi, I.Tavor, S.Hofstetter, S.Tzur-Moryosef, T.Blumenfeld-Katzir, and Y.Assaf. "Learning in the fast lane: new insights into neuroplasticity". In: *Neuron* 73.6 (2012), pp. 1195–1203. DOI: 10.1016/j.neuroimage.2010.03.004.

[122] Z.Tabanfar, M.Firoozabadi, Z.Shankayi, and G.Sharifi. "Screening of Brain Tumors Using Functional Connectivity Patterns of Steady-State Visually Evoked Potentials". In: *Brain Connect* 12.10 (2022), pp. 883–891. DOI: 10.1089/brain.2021.0170 (cit. on p. 61).

Web Pages

[19] *Andrew Penn . multicmp , MATLAB Central File Exchange., 2023,* URL: https://www.mathworks.com/matlabcentral/fileexchange/61659-multicmp (cit. on p. 32).

[26] *C.Ford,2017."The Wilcoxon Rank Sum Test." UVA Library StatLab.* URL: https://library.virginia.edu/data/articles/the-wilcoxon-rank-sum-test (cit. on p. 32).

[74] *Laplace Aproximation or Laplace Smoothing.* URL: https://www2.stat.duke.edu/~st118/sta250/laplace.pdf (cit. on p. 16).

[96] *Rik,2023.point to line distance, GitHub.* URL: https://github.com/thrynae/point_to_line_distance/releases/tag/1.3.2 (cit. on p. 33).

[97] *S. Kovács, T. Ruckstuhl, H. Obrist, and P. Bühlmann, "Graphical Elastic Net and Target Matrices: Fast Algorithms and Software for Sparse Precision Matrix Estimation," 2021,* URL: http://arxiv.org/abs/2101.02148 (cit. on p. 8).